ECOLE POLYTECHNIQUE FEDERALE DE LAUSANNE
SCHOOL OF LIFE SCIENCES

Master's project in Bioengineering and Biotechnology

Effects of Tissue-Level Ductility on Trabecular Bone Strength

Carried out in the laboratory of Orthopeadic Biomechanics

at the University of California Berkeley

Under the supervision of Professor Tony M. Keaveny

Done by

FREDERIC JUILLARD

Under the direction of

Prof. Dominique Pioletti

In the Laboratory of Biomechanical Orthopedics

EPFL

LAUSANNE, EPFL 2011

ABSTRACT

Osteoporosis is one of the most common skeletal diseases that lead to an accelerated bone loss due to an imbalance in bone turnover [2]. This low bone mass and degraded bone microarchitecture cause a reduction in mechanical properties and an associated increase in fracture risk [3]. If individual trabeculae become more brittle with aging, disease, or drug treatment, how does that influence the strength of the overall trabecular bone? This multi-scale issue, which relates energy absorption or tissue ductility at one scale to load-carrying capacity or strength at a higher scale, is particularly relevant in osteoporosis applications since it is well known that aging and drug treatments can influence tissue-level ductility [42]. However, the link between tissue ductility and apparent-level strength for trabecular bone is poorly understood and thus is it not currently possible to infer how known changes in tissue ductility translate into the higher scale and more clinically relevant changes in trabecular strength. To provide insight into this issue, our goal in this study was to determine how trabecular strength is altered when the tissue is changed from perfectly brittle to perfectly ductile — the two extremes of possible tissue-level ductility.

The results show that overall trabecular strength can vary two-fold if the tissue is entirely brittle compared to entirely ductile. The comparison with the experimental data suggests that at low bone volume fraction, real variations in tissue ductility could be important since the real behavior is situated between the ductile and brittle behaviors. If so, this implies that future studies assessing the structural consequence of changes in tissue-level ductility need to consider the bone volume fraction.

Our analyses are unique since they are the first to account for the complex 3D geometric detail of real trabecular microarchitecture and this study is the first to mechanistically link tissue-level ductility, a potentially important aspect of tissue material behavior, to the apparent-level strength, which is relevant clinically.

ACKNOWLEDGMENTS

I would first like to thank my advisor, Professor Tony Keaveny, who taught me everything I know about bone biomechanics, and for giving me the opportunity to perform my Master's Thesis at U.C. Berkeley and work in the Orthopaedic Biomechanics Lab. I would also like to recognize my thesis committee members Professor Dominique Pioletti and Doctor Alexandre Terrier who have been a source of guidance, encouragement and motivation. As well, I want to thank my fellow workmates of the Orthopaedic Biomechanics lab for their patience in passing on their knowledge. Thanks most of all to Shashank Nawathe who spent hours supporting me throughout computational scripts difficulties and mechanic phenomena interrogations. Finally, I want to thank my family and friends. Mum and Dad, thank you for your unconditional love, support and encouragement. We have been trough a tough time, but I finally did it. I owe a huge dept of gratitude to all my school companions at UCB and EPFL. You guys provided me lots of fun, and I would probably never be who I am today without your support, inspiration, and friendship. A last special thank to Laura who convinced me to come to UCB. I probably spent the craziest moments of my life thanks to you. I take you as a model regarding the ambition you have and the way you boss your life. Hopefully our friendship will last for life.

TABLE OF CONTENTS

1. INTRODUCTION

While the skeletal system in a healthy individual is outstandingly long lasting and well adapted to perform a large range of activities, bone fractures are a significant health concern, as they occur most commonly in the elderly where there are devastating consequences on morbidity and mortality [1]. It has been estimated that at least 20% of women have suffered one or more fractures by age 65, and as many as 40% suffer such fractures after the age of 65 [2]. Bone fragility can increase as a result of age- or disease-related changes, leading to a higher risk of fractures [1]. There are several possible reasons for increased fragility, but the most predominant is osteoporosis, which usually occurs in post-menopausal women and aged people [1].

Osteoporosis is one of the most common skeletal diseases that lead to an accelerated bone loss due to an imbalance in bone turnover [2]. This low bone mass and degraded bone microarchitecture cause a reduction in mechanical properties and an associated increase in fracture risk [3].

Annual costs in the United States are evaluated at 19 billions $, for a total of 2 millions fractures related to osteoporosis, and these figures are supposed to augment as the elderly population pursue its expansion [4]. Common locations for these fractures are the proximal femur, distal radius, and vertebral body. Problems related to the broken bone itself or the surgery usually induce an acute degradation in quality of living, and even the death of 20% of seniors within a year following fracture [4].

Osteoporosis is known to be associated with a decrease in bone quality. Bone quality involves all parameters beyond bone volume fraction (bone density) that can impair fracture risk, such as collagen cross-linking, bone architecture and hard tissue material properties [5, 6]. If these small-scale properties have a role on fractures, they consequently must have a biomechanical effect at a higher hierarchical structural level. Assessment of the material properties of trabecular hard tissue is necessary to figure out the effects of treatment, aging, and disease on bone fragility at the tissue level as well as the integrated effects at higher scales. For example, antiresorptive drug therapies can substantially attenuate fracture risk, although biomechanical consequences of these therapies at the tissue-level are not clear [7, 8].

As far as trabecular bone is concerned, very little understanding of how small-scale properties affect trabecular apparent strength has been displayed. We believe that tissue-level post-yield properties, also known as ductility, may have a potential role on the apparent-level strength behavior. It is reasonably evident that the question: " What is the strength of trabecular bone?" is not easily answered because of the heterogeneity of this parameter. It is essential to first specify details such as anatomic site, species, age, and disease state [1]. One approach to gaining insight into the role of tissue-level ductility on trabecular strength is to use Finite Element Analysis models built from 3-dimensional micro-Computed Tomography images, which inherently capture structural information of trabecular microarchitecture.

Apparent density of bones, also said as bone volume fraction (BV/TV), is the principal factor for estimating trabecular bone mechanical properties [9]. Indeed, bone volume fraction can veritably account for 70 to 90% of variations in apparent strength within a single anatomic site [10]. In the context of this thesis, factors that contribute to bone strength but are not accounted for by measures of bone density are termed bone quality factors (Figure 1.1).

The topic of bone quality has accumulated most of its consideration in the context of osteoporotic fracture and therapeutic treatments for osteoporosis. Researchers have observed that decreases in fracture risk due to therapeutic treatment cannot fully be explained by increases in bone mineral density alone [11-13]. Osteoporosis is commonly diagnosed using an areal measure of bone density, predetermined by dual energy X-ray absorptiometry (DXA). Unfortunately this technique is not very successful regarding the large range of anatomic sites [14]. Moreover, a recent study revealed that most patients who experienced fractures throughout a seven-year trial had DXA scores beyond the osteoporotic range [15], indicating that the technique cannot thoroughly account for decreases in fracture risk related to increases in bone density [11, 13]. Consequently, it is suggested that bone quality effects, such as material properties, contribute aside to fracture risk [5, 6]. This is due to factors such as immoderate trabecular thinning or loss of connectivity, which are considered to induce trebeculae to fail by mechanisms such as large-deformation bending or buckling [17, 18]. The loss of trabeculae in osteoporosis is more damaging for the overall structural integrity and strength of a trabecular bone structure than thinning of the trabeculae because lamellar new bone can only form on

existing surfaces.

In opposition to the empirical nature of DXA technique, high-resolution finite element models can provide a mechanistic assessment of bone strength. Although these FE models have not been considered in a clinical context yet, they already demonstrated to provide relevant information on bone fragility that cannot be acquired by microarchitectural or bone density measurements alone [14, 19, 20].

Previous high-resolution finite element models studies have demonstrated that effects of large-deformation failure mechanisms on trabecular strength should be insignificant in high-density bone [21-24]. Cellular solid theory predicts that high-density trabecular bone likely fails by tissue-level yielding, and that low-density bone likely fails by excessive bending or buckling, consistent with the form of strength-density characteristics observed in experimental studies [25].

One key issue in bone biomechanics is the influence of tissue-level ductility on the overall strength of trabecular bone. If individual trabeculae become more brittle with aging, disease, or drug treatment, how does that influence the strength of the overall trabecular bone? In the present study, we seek to narrow the in vivo overall structure behavior of trabecular bone failure properties by investigating both extremes behaviors with high-resolution FE analyses, known as perfectly ductile and perfectly brittle. We can contribute to the comprehension of etiology of osteoporotic fracture and the mechanisms by which drug treatments moderate fracture risk by assessing the effect of these types of failure mechanisms and associating them to bone density.

The type of perfectly brittle modeling is often used in analysis of structures to identify those parts of the structure that are critical to overall stability. Ideally, if the post-yield behavior of the bone tissue were well characterized, we could incorporate that combined yield-fracture behavior into the finite element models. But these properties are not well characterized for trabecular tissue. Thus, our double-barreled approach modeling fully ductile and fully brittle extremes separately represents a feasible and unique means of both linking tissue post-yield behavior to overall structural behavior and assessing locations of the weak-link regions [42].

We consider 21 high-resolution finite element models corresponding to cubic specimens (5mm edge) of trabecular bone on which 1% apparent strain is applied in compression for both fully brittle and ductile material behaviors at the tissue-level. We wish to

investigate failed tissue amount and locations at highest risk of initial failure to enable the visualization of damage progression within a specimen, when the load is maintained. By using high-resolution finite element models based exclusively on trabecular bone strength, this study provides unique insight into tissue-level ductility related to apparent-level strength.

1.1 Bone Composition and Structure

There are two basic types of bone tissue. Cortical, or compact bone is the densest bone in the skeleton and is located in the diaphysis, or central shaft, of a long bone such as the femur (Figure 1.2). Trabecular, or spongy bone, is much less dense than cortical bone and is usually found in the epiphysis regions at the end of long bones.

Bone has unique material properties and, like almost all biological tissues, it has the ability to repair itself and adjust to changing environmental conditions by structural adaptations [26]. With aging and disuse, bone tissue is resorbed, resulting in substantial losses of tissue stiffness and strength [1].

Bone consists of both living tissue and non-living substances. On a volume basis, bone is around 40 percent inorganic, 35 percent organic and 25 percent water [1]. The inorganic phase of bone are crystalline salts composed principally of calcium and phosphate, referred to as hydroxyapatite: $Ca_{10}(PO_4)_6(OH)_2$. They are deposited on a collagen fibers matrix [15]. Collagen fibers of bone provide great tensile strength and flexibility, while the calcium salts, similar in physical properties to marble, have great compressional strength, which gives bone its toughness and rigidity.

That composite of mineralized collagen fibrils (~30 nm diameter x 300 nm length) represents the lowest level of bone tissue (Figure 1.3). At the next level, these fibrils are arranged either as stacked thin sheets called lamellae that contain unidirectional fibrils in alternate angles between layers or as a block of randomly oriented “woven” fibrils [1]. These lamellae can be organized as large concentric rings wrapped around a central Harvesian canal, which encloses blood vessels, nerves and bone cells. This structure, called an osteon, has a diameter of about 200 microns and length of 1-3 mm [14]. It represents the primary unit of human adult cortical bone and is continually being

broken down and replaced by the numerous types of cells in a biological process called bone remodeling [1].

Cortical bone tissue is made of an osteonal microstructure that results in transversely isotropic material behavior, meaning that its material properties depend on the loading direction [1]. Transverse isotropy can be defined by a direction having properties different from those in a mutually perpendicular plane [1]. Cortical bone is stronger in compression than in tension, and stronger (and stiffer) for longitudinal than for transverse loading [1]. Its elastic modulus and strength can vary almost twofold because of its variable porosity, which has the tendency to increase with age [1]. The primary difference between cortical and trabecular bone is porosity. In humans, cortical bone is typically 5-30% porous while trabecular bone is an extremely heterogeneous material due to its porosity that ranges from about 60-95 percent. The details of trabecular bone morphology and mechanical properties will be addressed in a further section.

1.1.1 *Bone Adaptation*

The human skeleton constantly experiences the processes of growth, reinforcement, and resorption and has a remarkable ability to repair itself after injury [25]. Even more impressive is the ability of bones to adapt to their mechanical demands placed on it by daily activities, thereby producing structures that are optimized for their functional operating conditions [1]. The bone structure can adapt in both the geometry and material properties in response to mechanical loading [1]. This phenomenon is called adaptive capability. A feedback is provided by the bone cells serving as both sensors (detecting changes in the mechanical environment) and actuators (causing bone tissue to be deposited or removed) [1].

1.1.2 *Bone cells* (Figure 1.4)

The growth, repair, and maintenance of bone are carried out by four types of cells that dwell bone tissue: osteoclasts, osteoblasts, osteocytes, and bone lining cells [26].

The osteoclast is a giant cell that dissolves bone surface by removing its mineralized matrix and breaking up the collagen network [27]. This process is termed as bone resorption. Osteoblasts are specialized fibroblasts that secrete a matrix of osteoid, later mineralized to form bone. The coordinated action of multiple osteoblasts determines

which type of bone tissue is developed. Osteoblast cells tend to decrease with age, affecting the balance of formation and resorption in the bone tissue [27].

When osteoblasts become trapped in the matrix they secrete, they differentiate into osteocytes [26]. The body of the cell occupies the lacunae, whereas its processes elongate through the half-micron diameter canaliculi and connect to other osteocytes at gap junction [1]. It is thought that the strain or some other mechanically induced input signal may be detected by these cells and transduced into a chemical signal that then generates bone remodeling by osteoblasts and osteoclasts [1].

The bone lining cell is a dormant osteoblast. These cells cover 90 percent of the trabecular bone surface and line the surfaces of all bones and the Haversian canals [1]. They extend projections that connect osteoid to osteocytes and attract the latter towards damaged areas for repair.

1.2 Trabecular Bone Morphology and Mechanical Properties

Trabecular bone anisotropic microstructure consists of a number of interconnected rods and plates of irregular geometry, the degree of anisotropy depending on anatomic sites [1]. When trabecular bone is overloaded, its mechanical properties are greatly reduced, although the associated physical damage can be visually difficult to detect due to its widespread, but microscopic, nature. The rod and plate structures (trabeculae) are typically 100-300 μm thick in human bone, and are separated by larger marrow spaces with characteristic dimensions of 500-1000 μm [23,28]. Trabecular bone morphology and mechanical properties can vary greatly with age, anatomic site (Figure 1.5), and between individuals. The most important microstructural parameter for trabecular bone is its apparent density, in opposition to the tissue density of the individual trabeculae [1]. The apparent properties of trabecular bone primarily depend upon the architecture as well as anatomic sites and, to a smaller degree, on the tissue properties [1]. With aging or disease, architecture and density of trabecular bone is adapted, which results in thinning down individual trabeculae, generating a strength reduction. Strength varies with apparent density by a linear relationship with a slope being lower for the lower density sites [1]. This is due to differences in architectural structure: The plates for high-density bone are more efficient than the rods of lower density bone [1]. Originally, a typical apparent-level stress-strain curve for trabecular bone exhibits a relatively linear

elastic region for both tensile and compressive loading (Figure 1.6) [29]. However, yield and ultimate strengths in compression are considerably larger than in tension [30]. Tensile failure is characterized as brittle, while trabecular bone deterioration under compressive loading is significantly more ductile.

A unique characteristic in the mechanical behavior of trabecular bone is that apparent yield strains are rather uniform across a wide range of densities despite the considerable non-uniformity of modulus and strength [23, 31]. Yield strain provides unique knowledge on failure behavior since variations in yield strain illustrate changes in strength after accounting for differences in modulus. For low-density specimens, compressive yield strains are lower than those with high density. This is probably due to large deformation bending or buckling failure-type mechanisms of individual trabeculae. When the apparent density is low (< 0.25), the particular trabecula is inclined to be thinner and longer than for high-density bone, and this may support buckling as a failure mode, compared with material yielding. This excessive bending phenomenon does not occur for tensile loading.

1.3 High-resolution Finite Element Modeling of Trabecular Bone

High-resolution microstructural finite element models are built from micro-scale images of bone specimens with spatial resolution on the order of 5-100 μm. These images are essentially acquired using micro-scale scanning (Computed Tomography, Magnetic Resonance Imaging, etc.). In order to implicitly capture the microarchitecture of the specimen, finite element meshes are constructed using a technique called voxel-based conversion, in which each image voxel is directly transformed into an 8-node brick element [32]. High-resolution finite element models offer some clear advantages over experimental testing, defined as the gold-standard for assessing the mechanical properties of bone [33]. Since these models are non-destructive, the same specimen can be tested multiple times, which can thus considerably lower the number of specimens required to address biological heterogeneity [34]. Parametric variations can be made to the models such that the effect of individual parameters on bone properties can be examined in ways that are impossible to achieve in an experimental setting [35, 36]. Moreover, tissue-level stress and strain distributions can be assessed with these modeling techniques [37, 38]. Such information is helpful to investigate the deformation

and failure mechanisms in the bone specimen, as well as the locations at highest risk of failure [16]. Advances in imaging technology have enabled to generate in vivo high-resolution finite element models with voxel size of 80 μm, thus providing non-invasive estimates of bone strength and fracture risk in a clinical context [39, 20]. The main drawback of high-resolution finite element modeling is that the models have a large number of degrees of freedom ($\sim 10^5$-10^9) [33]. Consequently, analysis of the models typically requires specialized hardware and software. To enable the model to capture deformation mechanisms such as buckling and large bending deformation, the matrix stiffness is updated based on changes in the structure's configuration involved by geometric nonlinearities [33].

1.4 Justification for the Study of Trabecular Bone

This project focuses on the micostructure of trabecular bone, although fracture is an incident that arises at the whole-bone scale. However, considering the hierarchical nature of bone, in order to understand the mechanical behavior of the structure as a whole, one has to understand all component materials at all scales. From a clinical aspect, it is obvious that trabecular bone plays a role in osteoporotic fracture events since the most common fracture sites (such as the vertebral body, distal radius and proximal femur) are rich in trabecular bone [27]. Bone remodeling is altered by both osteoporosis and drug treatments. As trabecular bone is more biologically active than cortical bone, it is promising that disease and treatment have a greater effect on trabecular bone than cortical bone [33].

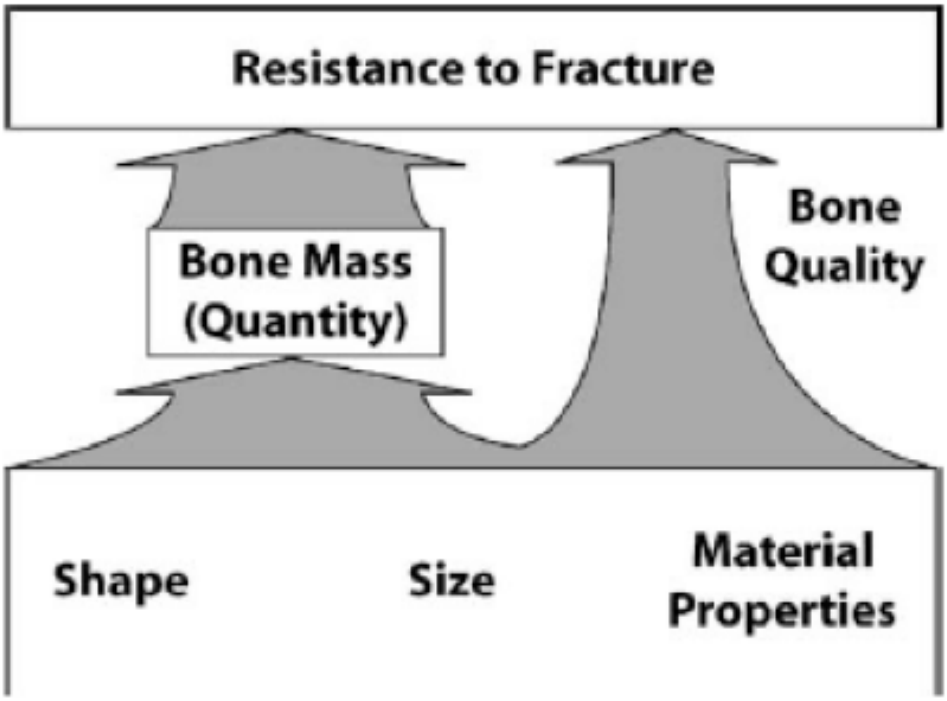

Figure 1.1. Schematic showing the role of bone quality in whole bone strength (fracture resistance). Factors that contribute to fracture resistance but are not accounted for by bone mass are considered to be quality effects. Adapted from [33].

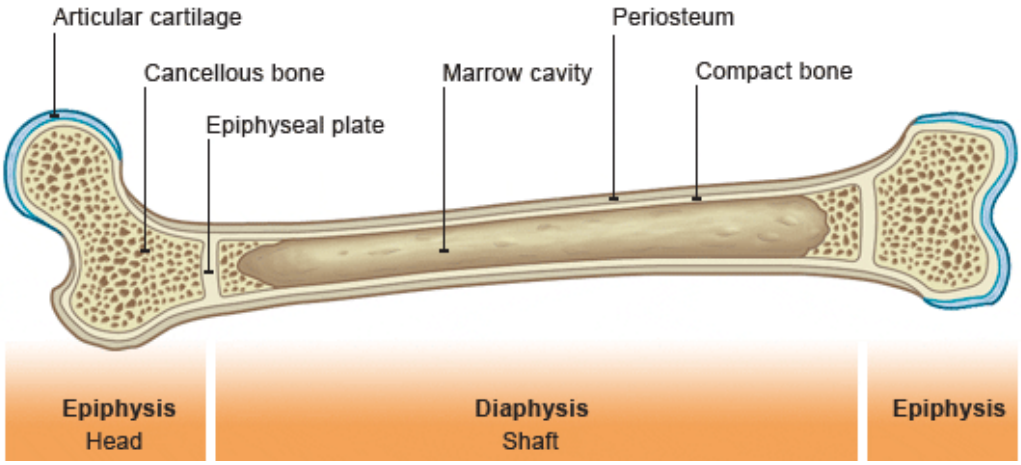

Figure 1.2. Composition of a Long Bone. Adapted from http://www.bbc.co.uk/schools/anatomy_skeleton

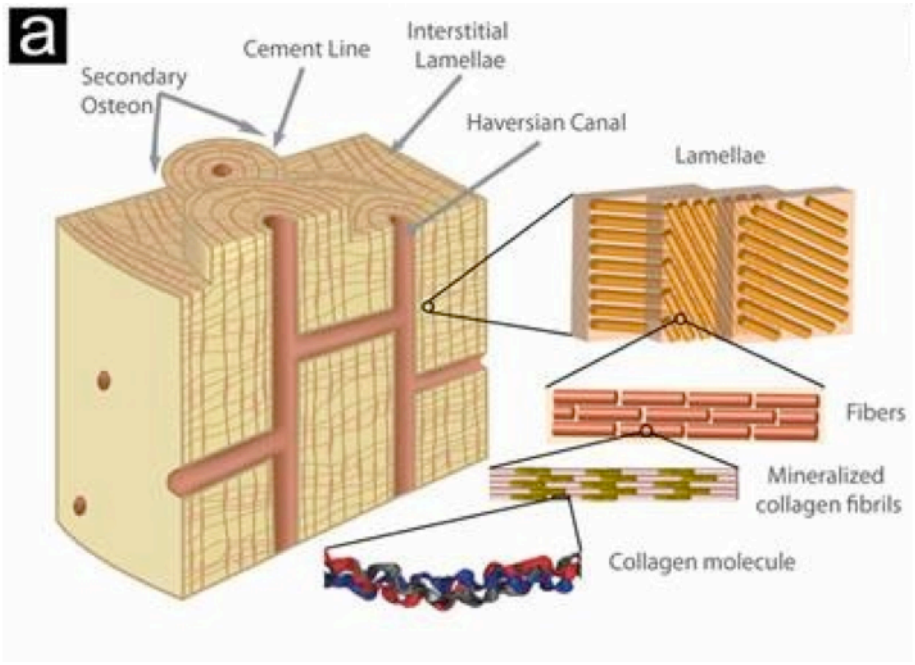

Figure 1.3. Microscopic structure of compact bone. Adapted from "The McGraw-Hill Companies, Inc."

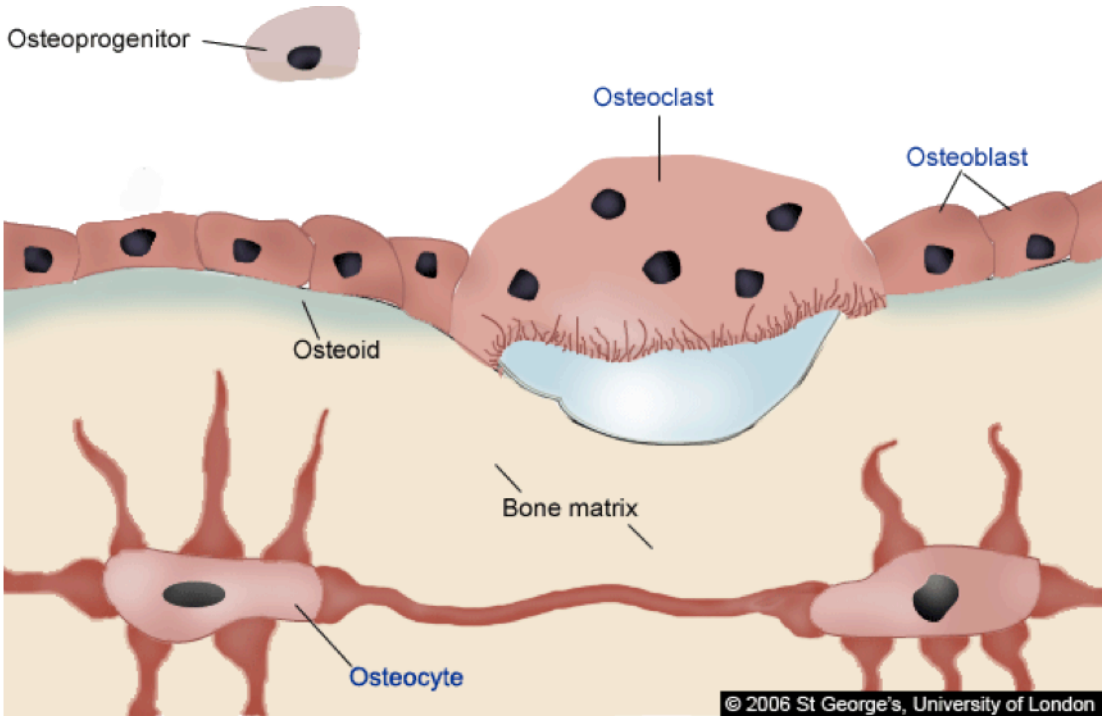

Figure 1.4. 4 types of cell dwell bone tissue: Osteocyte, Osteoblast, Osteoclast, and bone lining cell.

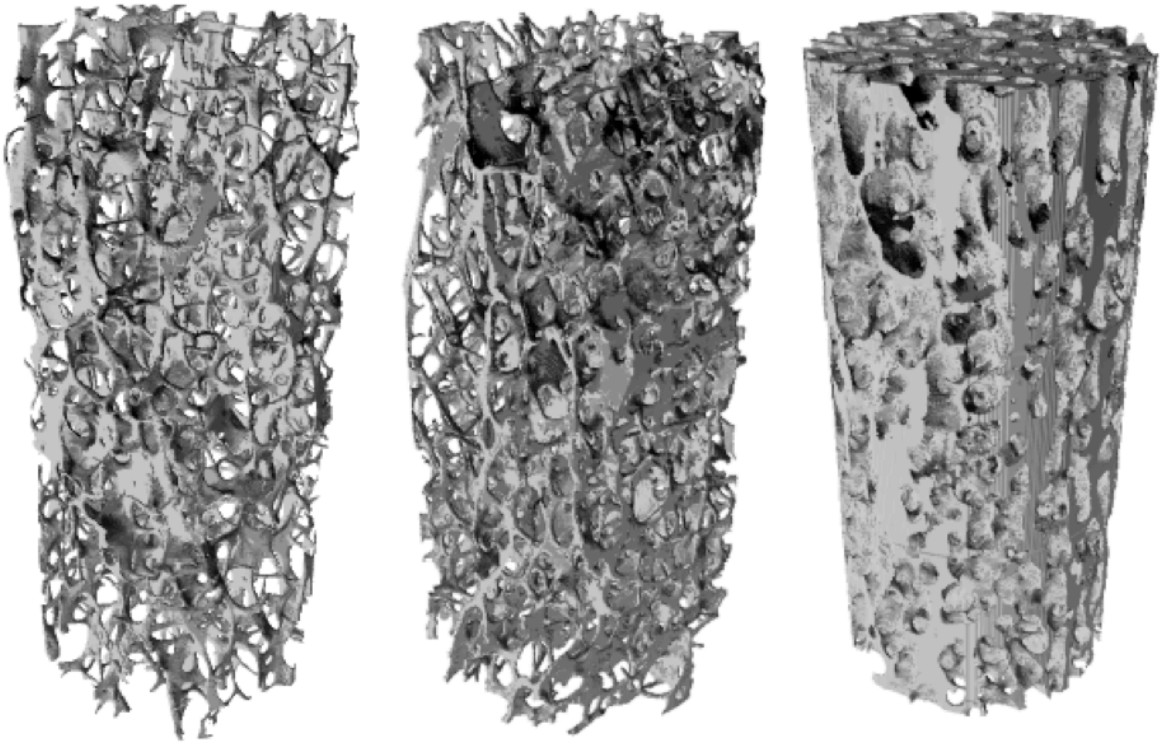

Figure 1.5. Trabecular bone cores (~8 mm diameter and 20 mm length) from the vertebral body (left), greater trochanter (middle), and femoral neck (right). The volume fractions of the cores are 6, 8, and 35%, respectively, demonstrating the substantial heterogeneity in porosity and architecture that can occur in cancellous bone. Adapted from [33].

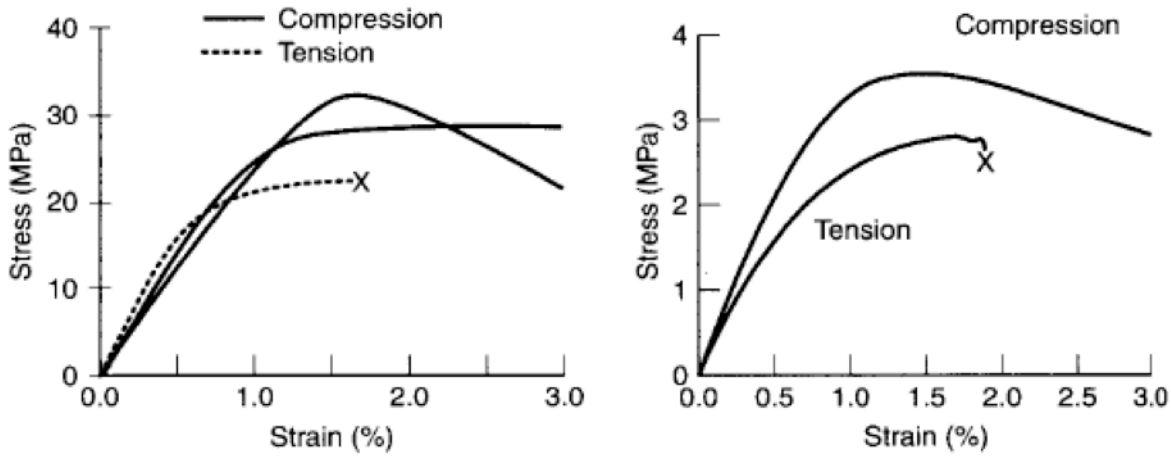

Figure 1.6. Typical stress-strain curves for high-density (left, ρ=0.65 g/cc) and low-density (right, ρ=0.20 g/cc) trabecular bone. Note that the strength and stiffness of the high-density bone is an order of magnitude greater than that for the low-density bone. Adapted from [33].

2. METHODS

2.1 *Study design*

We performed two different types of finite element analysis to assess effects of both extremes tissue-level material behavior known as perfectly ductile and perfectly brittle on the apparent trabecular bone specimen. For both tissue-level behaviors, we investigated failed tissue amount along with the analysis, as well as reactive strength evaluated at the whole bone scale at yield or ultimate point, respectively for ductile (nonlinear) or brittle (quasi-nonlinear) tissue-level material behavior. The reactive strength [N] corresponds to the pressure [MPa] required to reach a particular displacement, divided by the bottom surface of the cube [mm^2]. The yield point is defined as the stress at which a material begins to deform plastically, and the ultimate point corresponds to the highest point of the stress strain curve [1]. If additional load is applied further to the ultimate point, the whole specimen will collapse. Ductility is a solid material's ability to deform. It is the magnitude to which a solid material can be plastically deformed without fracture [26]. Brittle materials absorb relatively little energy prior to fracture, even those of high strength [26]. They break without significant deformation (strain) when subject to stress.

2.2 *Specimen Characterization*

Cubic cadaveric specimens (n = 21; 5mm edge) of trabecular bone were extracted from cylindrical samples (8 mm diameter, 20 mm length), selected from unpaired human proximal femurs (n=12), and vertebral bodies (n=9). The specimens covered a wide range in bone volume fraction (BV/TV range = 6-36%) and were taken from sixteen cadavers (age = 68±9.5; 10 male, 6 female). All samples were prepared with the principal trabecular orientation sensibly aligned with the axis of the cylinder [40]. Radiographic data confirmed that specimens were not damaged, and donors had no records of metabolic bone disease or cancer.

2.3 *Specimen Imaging*

High-resolution images were obtained by scanning the full cylindrical core of each specimen using micro-computed tomography (Scanco μCT 20; Scanco Medical AG, Brütisellen, Switzerland) at a spatial resolution of 20 (n = 8) or 22 μm (n = 13). Scans

were modified by segmentation in order to illustrate white pixels for bone tissues on a black background. Concatenating scans in the z-direction (total n=227 or n=250, respectively for 22 μm and 20 μm spatial resolution) generated three-dimensional volumes.

2.4 *Finite Element Analysis*

A three-dimensional finite element model for each specimen was generated from a three-dimensional CT volume by converting individual voxels into eight-node brick elements [32]. The resulting finite element models contained up to 4.5 millions elements and over 15 millions degrees of freedom each.

For the perfectly ductile material behavior analysis, a nonlinear elasto-plastic behavior at the tissue-level (Figure 2.1) was homogeneously attributed to the models with an isotropic elastic modulus of 18 GPa and a Poisson's ratio of 0.3 [16]. At the tissue-level, asymmetric tensile yield strain of 0.33% and compressive yield strain of 0.81% were calibrated for all models [41]. Consequently, as soon as an element starts yielding, it is assumed as failed and its elastic modulus is 100 times decreased in order to account for damage. We chose a 100-fold decrease because we wanted to make the elastic modulus significantly less for damaged tissue to be structurally much less relevant than the intact tissue. Applying displacement at the top surface and roller-type boundary conditions at the bottom surface simulated a compressive type of loading.

Numerical analyses were performed on a Sun Constellation Linux Cluster (Ranger, Austin, Texas). Using 64 processors in parallel, a run time of approximately 20 minutes was required for each analysis, amounting to 420 minutes for the 21 specimens. The outcome variables from each simulation were apparent stress and amount of failed elements in tension and compression within 20 intermediate steps (established at each multiple of 0.05%) for a final apparent level strain of 1%.

Similarly, for the perfectly brittle behavior at the tissue-level (Figure 2.2), a quasi-nonlinear approach was used in which elements were effectively removed (elastic modulus reduced 100-fold) once either the tensile or compressive strength (respectively 59.8 N and -145.8 N) at the tissue level was exceeded and a new analysis was then performed to an incrementally higher displacement. Three-dimensional finite element models were generated from three-dimensional CT volumes. Material

properties, as well as asymmetric tensile-compressive yield strains were assigned in a similar manner as in ductile models, however failure was modeled in a different way. In opposition to the ductile behavior model wherein load was applied simultaneously in one process from 0 to 1% apparent strain, the brittle method was formed out of 20 linear analyses for which the procedure always started at 0% and stopped at a multiple of 0.05%, gradually increased until 1% apparent strain was reached at the last step (Figure 2.3). To illustrate damage, elements exceeding the tissue-level fracture strain in tension (0.33%) or compression (-0.81%) after each step encounter a 100 times elastic modulus reduction. Accordingly, these elements were considered as failed, and starting the next step from 0% apparent strain with updated tissue-level elastic properties mimics the brittle behavior. Total CPU time was approximately 6840 minutes, equivalent to about 30 minutes in real time since 228 processors in parallel were required for each analysis. According to this, 800 minutes were necessary for one specimen, and thus 16800 minutes for all of them.

2.5 *Computational Steps*

In brittle tissue behavior analysis, we first created on the local computer a FEAP file (text file) on the basis of the three-dimensional FE volume, which considered a specific apparent compressive strain value corresponding to a particular step. This FEAP file contained a list of all bone elements and their corresponding 8 nodes 3D coordinates, as well as displacement conditions in z-direction for top surface elements. The FEAP file was sent to the supercomputer for mechanical simulation. Three main outcomes were obtained: the reactive strength at the apparent level, and two "sig" files containing 3D coordinates of each element and their corresponding 6 strain values (σ_{xx}, σ_{xy}, σ_{xz}, σ_{yy}, σ_{yz}, σ_{zz}). The first "sig" file involved non-failed elements (according to tensile and compressive strain criterions), and the second one failed elements. These "sig" files were sent to the local computer for post-processing. Considering these extra failed elements, a new FEAP file could then be created to continue with the next step, and locations of failed elements in tension and compression were accounted. Figure 2.4 represents a chart with main steps of the brittle material behavior analysis, and appendix 5.1 is a descriptive of the main steps.

Regarding the ductile analysis, only one step (corresponding to 1% compressive displacement) was required. The FEAP file was created on the basis of the 3D FE

volume. It was then sent to the supercomputer for mechanical simulation, and apparent strength, as well as locations of failed elements could be recorded at multiple intermediary steps. Appendix 5.2 describes the main steps of the fully ductile FEA.

2.6 *Analysis of data*

For the ductile material behavior model, the apparent yield point was determined from the apparent stress-strain curve of each specimen using the 0.2% offset method [16]. However, for the brittle model, the ultimate point was established by the local maximum arising on the apparent stress-strain curve. We define the apparent stress corresponding to the ultimate strain as brittle strength. In like manner, ductile strength is illustrated by the apparent yield stress obtained in ductile analysis. Apparent Young's Modulus is defined as the slope of the initial, linear portion of stress-strain curves at apparent level.

In order to observe tensile and compressive failure progression, specimens imaging, in x-z plan according to Figure 2.5, was performed for each of the 20 steps of the analyses (GIMP, version 2.6, Kimball, Mattis). These images provide important information on locations of the weak links. For each step, 10 slices of the x-z plan were concatenated to get 22 or 25 sections (respectively for 22 and 20 μm spatial resolution) of a unique specimen. Different colors were attributed to elements failing either in tension (red) or compression (green). In the specimen, a unique section (out of the 22 or 25) was selected according to its information contribution at each one of the 20 steps (distinct by the displacement incrementally increased by 0.05%), and animations on the damage progression were realized.

To give insight into both finite element models predicted values, stress and strain values calculated at the whole specimen scale were compared with experimental results from cylindrical specimens (8 mm diameter, 20 mm long) gathered at yield point (defined by the 0.2% offset method). First, FE predictions of yield or ultimate strength (respectively for ductile or brittle behavior) were plotted against the experimentally measured values for all specimens. The errors in the FE predictions were assessed using a paired t-test (JMP, version 8.0, SAS Institute Inc., Cary, NC) to determine if the error was statistically different from zero. This procedure was also repeated for the error in the prediction of yield or ultimate strain for each specimen, since strain represent a more rigorous

statistical test than stress, given the wide variations in stress typically seen across specimens [19].

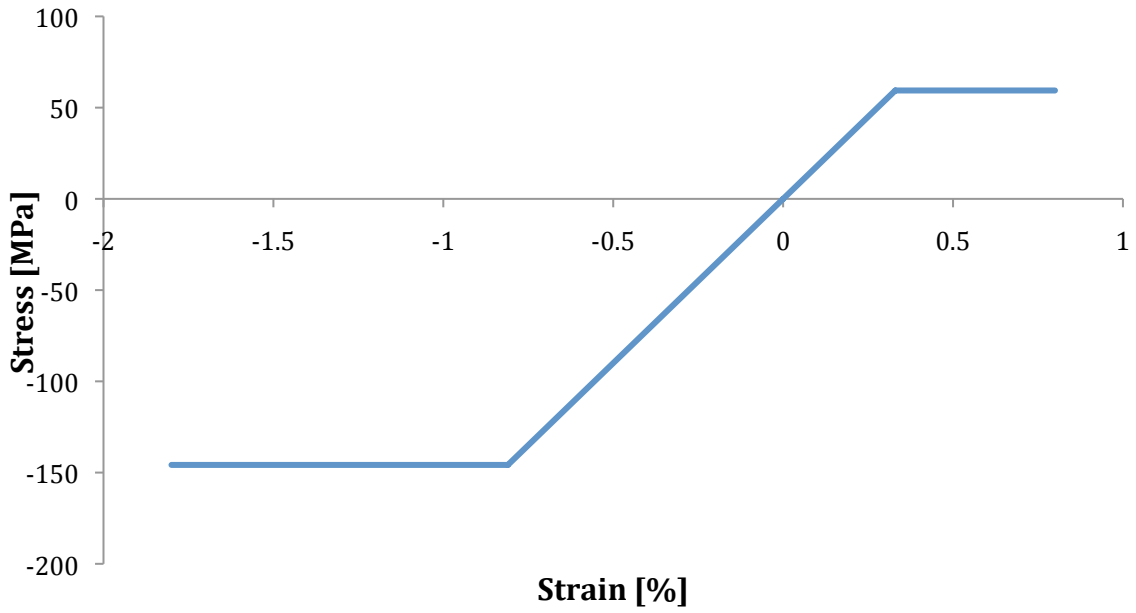

Figure 2.1. Tissue-level stress-strain curve for perfectly ductile material behavior exhibits an elasto-plastic behavior.

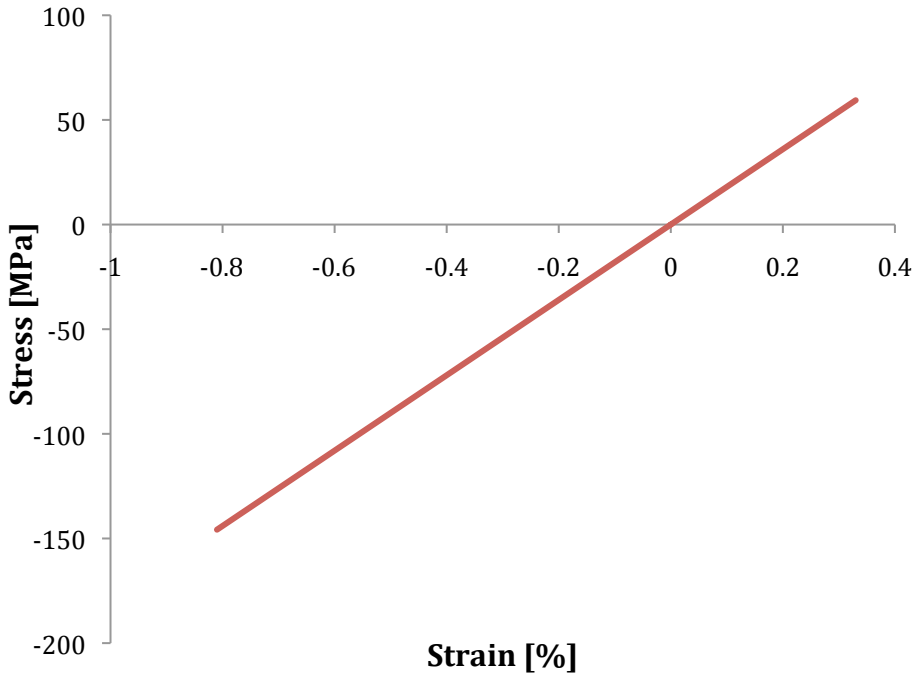

Figure 2.2. Tissue-level linear stress-strain curve for fully brittle material behavior exhibits a fully elastic behavior until failure.

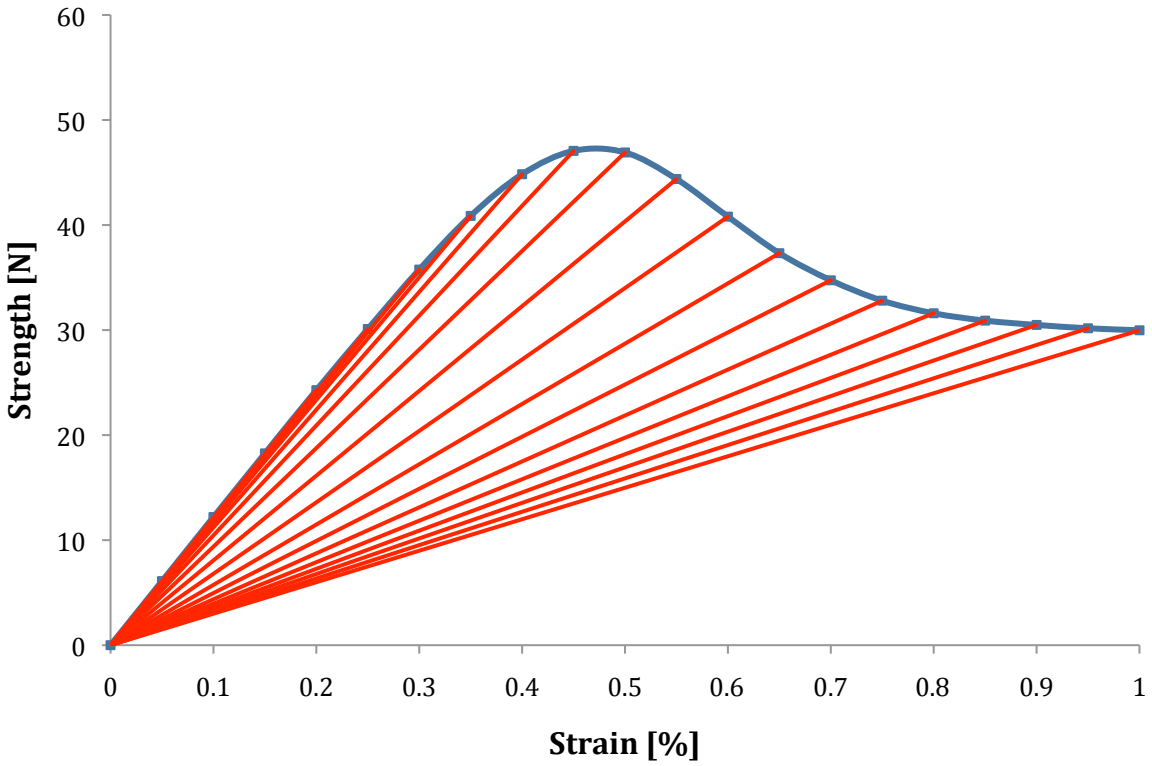

Figure 2.3. Tissue-level brittle material behavior analysis consists in twenty linear analyses. Apparent strain is incrementally increased from 0 to 1% and the main outcome is the corresponding strength.

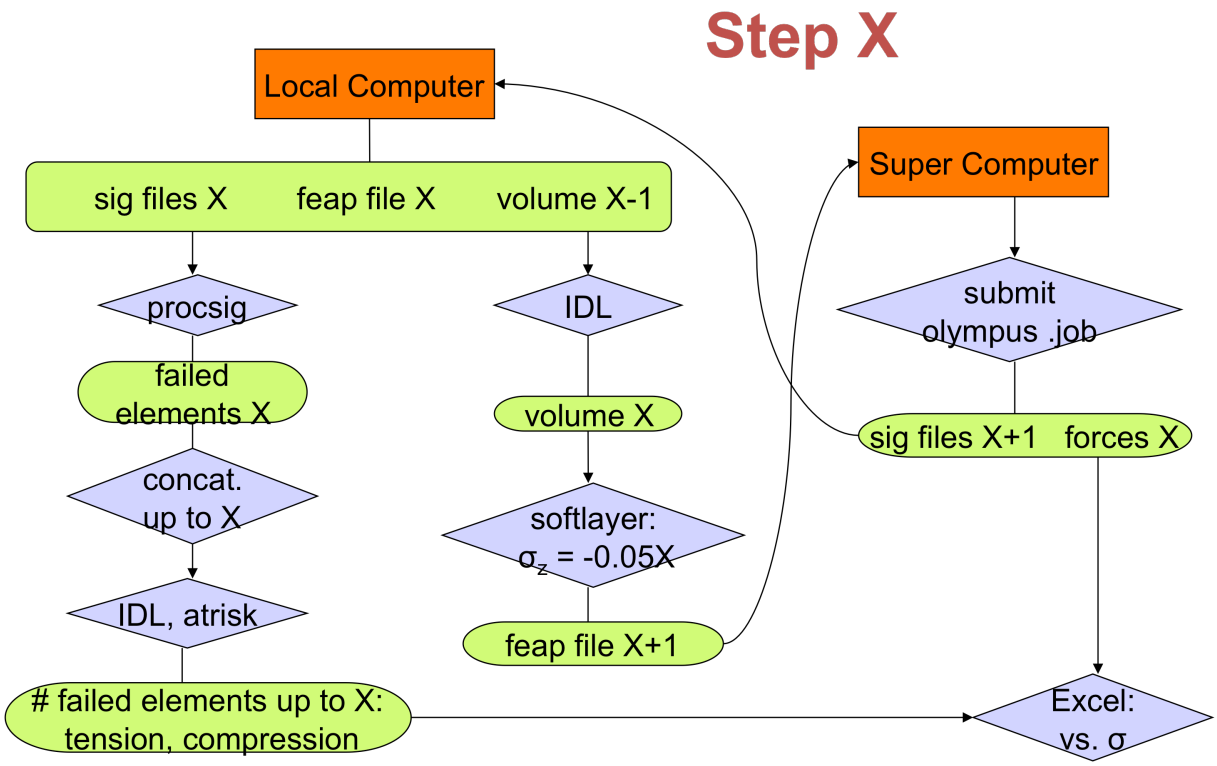

Figure 2.4. Brief summary of main procedures and required files or scripts for one particular step in the brittle material behavior analysis.

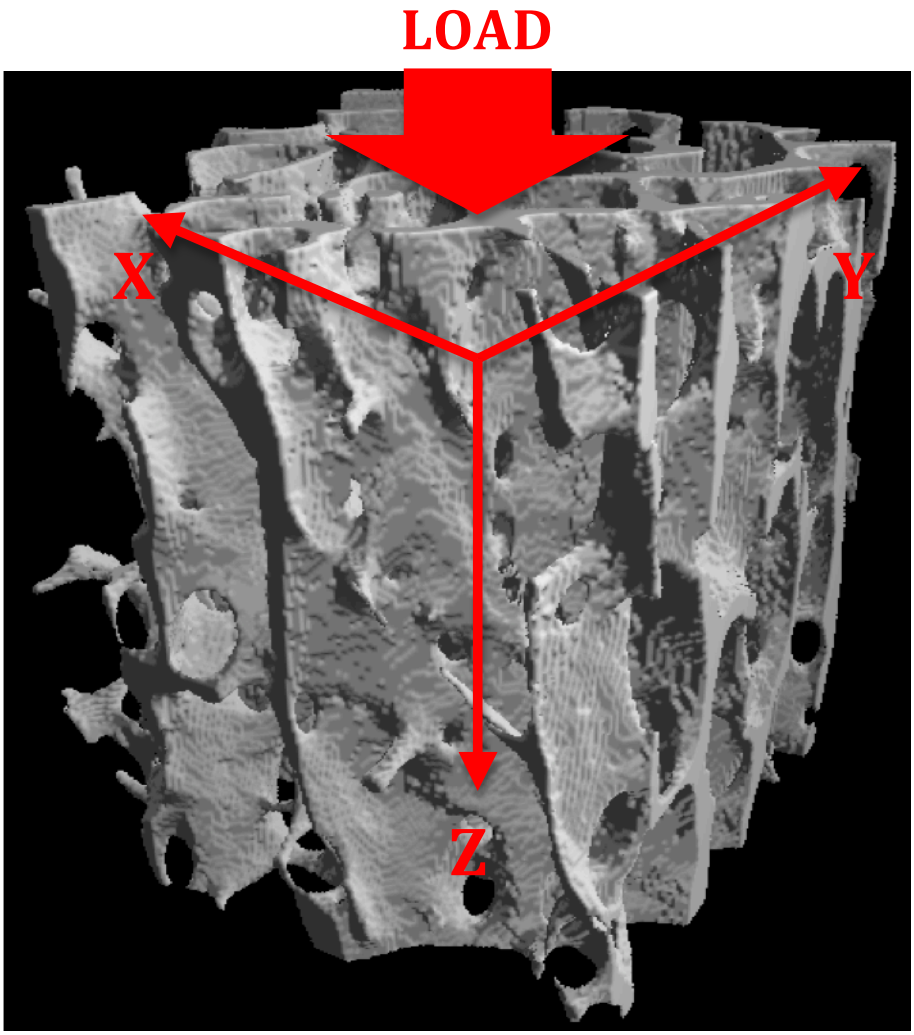

Figure 2.5. X-, Y-, and Z-directions referred to specimen imaging. 10 layers in Y-direction are concatenated in order to visualize a 220 μm thick slice of the specimen in the X-, Z- plan, which corresponds to trabeculae tissue thickness.

3. RESULTS

3.1. *Strength Predictions*

Graphs displayed on Figure 3.1 show stress-strain curves at the apparent level, predicted by the "perfectly ductile" and "perfectly brittle" FE analyses. This type of graph has been realized for all specimens and the present ones have been selected in order to demonstrate the results variability depending on bone volume fraction (BV/TV).

Brittle and ductile strength values and their corresponding strains have been collected in order to compare both analyses, and to give insights about sample material properties and bone volume fraction dependence. To give insight into BV/TV dependence with the stress-strain curve characteristic form, one can modulate strength values with the yield strength (from ductile FEA) of the specimen (Figure 3.2). On the basis of this figure, we observe an identical shape of stress-strain curves across a large variety of bone volume fraction for both ductile and brittle material behaviors. We notice the common trajectory of both FE-analyses during the first 5-7 steps, in which a negligible amount of tissue fails. As tissues start to fail, the brittle analysis deflects from the common trajectory and reaches its ultimate point very quickly. This point is defined by the local maximum on the curve, and signifies that if additional load is applied on the whole specimen, the latter will completely collapse.

Considering Figure 3.3, for both ductile and brittle analyses, there was a strong correlation between strength and bone volume fraction (R^2>0.96). These two parameters are highly dependent (p values < 0.0001). Experimental results were gathered from trabecular cylinders (8mm diameter, 20 mm long) with different BV/TV from our samples. Despite the impossibility to match them with our specimens, we observe that they tend to follow the ductile analysis for specimens with BV/TV above 0.2. The 3 sets of data are very close to each other at low bone volume fraction.

3.2. *Brittle vs. Ductile Tissue-Level Behavior*

As a result of the similarity of these relations, the ratio of ductile to brittle strength (mean ± SD = 1.79 ± 0.04) was remarkably constant across all specimens (Figure 3.4). This mean ratio implies that enabling a ductile behavior causes the apparent strength to almost double. However, we remark that ratios are less for high BV/TV specimens than

for the low BV/TV ones. Despite the considerably diffused distribution of data, the p value equals to 0.008 reveals the dependence between these ratio values and BV/TV.
With reference to strain-BV/TV dependence, we remark a slight increase of ultimate or yield strain with BV/TV increases (Figure 3.5). The ductile FE analysis slope is however higher than the brittle one, whose strain values only vary from 0.4 to 0.5. P values for brittle and ductile FE analyses are equal to 0.0001 and 0.0002 respectively. Experimental data represent a similar range of bone density than FE analyses. Beyond densities of 0.2, strain values are comparable to the ductile analysis. The slope of the recurrence curve adapted to experimental data is however rather high because of low BV/TV specimens whose corresponding strains are situated between the two FE-analyses predicted values.

3.3. *Young's Modulus*

Apparent Young's Modulus can be observed on Figure 3.1. Since initial fractions of both ductile and brittle tissue-level material behavior curves are identical, both models possess the same Young's Modulus. We denote (Figure 3.6) a highly dependence between Young's modulus and BV/TV (p value < 0.0001). Indeed, the higher the BV/TV, the steeper the gradient of the stress-strain curve.

3.4. *Assessment of Failed Tissues*

The second main outcome is the assessment of failed elements. These values were processed in order to give insight into failed tissues as a percentage of the total amount of bone tissues for a particular specimen.
Figure 3.7 shows tensile and compressive cumulative percentage of failed elements from 0 to 1% apparent strain. At each step, failed elements are accounted and added to the previous step amount. For the ductile analysis, we remark an increasing gap between tension and compression while BV/TV augments. This is mainly due to the dependence between elements failing in compression and BV/TV, whereas tensile curves barely differ between specimens. More tissues fail under tension in low BV/TV specimens, and as the density pass 0.1, compression becomes the main process of failure. These functions adapted an exponential curve, while in the brittle analysis; both tensile and compressive behaviors tend to have a sudden increase at ultimate strain and a slight decline a few steps later. Contrarily to ductile analysis, more tissues fail under tension

across the range of densities. However we notice more elements failing under compression in the specimen with highest BV/TV. These graphs were realized for each specimen, and values were gathered at 1% apparent strain, and at yield or ultimate point (respectively for ductile or brittle tissue-level material behavior).

Considering the cumulative percentage of failed elements until yield or ultimate point (Figure 3.8), the main point to denote is the huge gap between the two FE expected values. Indeed, much less elements are failing in the brittle mechanic behavior because the ultimate point is reached at very low strains. We notice the dependence of both FE analyses predicted values with BV/TV (both p values < 0.0001). However the slope of the brittle recurrence curve is far lower than the ductile one.

Concerning the percentage of failed elements in tension, we deduce from Figure 3.9 that ductile model does not depend on BV/TV (p value = 0.74), whereas the brittle one does (p value = 0.0021). These two sets of data, gathered at 1% apparent strain are very close to each other compared to compressive values in Figure 3.10. Despite the dependence of tissue-level brittle behavior model with BV/TV, both FE analyses exhibit very few variations across specimens compared to Figure 3.10. Indeed, there is obvious dependence between amounts of elements failing under compression with BV/TV for both FE analyses. For tissue-level ductile behavior, there is approximately 20% of total amount of elements that fail for specimens with BV/TV beyond 0.2%, whereas the latter is always less than 5% for the brittle model.

Regarding these tensile and compressive data at 1% apparent strain, we notice that tissue-level ductile behavior model always predict more failed elements than the brittle one. Ratio values depicted on Figure 3.11 decrease as the BV/TV increases, which can be observed on Figure 3.9, but that phenomenon is not obvious from Figure 3.10. These ratio data decrease, as large deformation impacts are less important, indicating that tissue-level brittle material FE analysis predicts values closer to ductile ones as BV/TV increases. It is interesting to observe that both recurrence curves possess similar slopes.

Considering the cumulative percentage of failed elements until 1% apparent strain, tissue-level brittle material behavior model has a higher ratio between tension and compression than the ductile model (Figure 3.12). However, according to BV/TV increases, ratios for both analyses decrease, indicating that more and more elements fail in compression, while tensile ones do not vary as we could notice on Figure 3.9.

Dependence between these data and BV/TV can be observed (p values < 0.0001), and a logarithmic recurrence curve shows better R^2 values than linear does.

3.5. *Maximal Incremental Damage*

Figure 3.13 exhibits incremental percentage of failed elements at each step, without adding previous step quantities, contrarily to cumulative values displayed on Figure 3.7. For low BV/TV specimens, initial elements fail under tension, while they tend to adopt a compressive failure mode for specimens with higher BV/TV. Tensile and compressive curves tend to move closer as sample's BV/TV increases. In the brittle model, these predicted values always reach a local maximum after the ultimate point, whereas in the ductile behavior analysis, that local maximum constantly arise before the yield point. The negative gradient following local maxima of both curves is higher in brittle than in ductile curves. However, compressive values predicted by the ductile model are subject to a higher decrease after maximum than tensile ones. Tension values across the range of densities do not vary much (as observed on Figure 3.8), which can explain why the higher the BV/TV, the more distant tensile and compressive curves are.

These graphs have been made for each specimen. We added tensile and compressive predicted values to estimate local maximum values (defined as Maximum Incremental Damage, MID) for both FE analyses, as well as their associated apparent strain. Estimated MID apparent strains, as well as ultimate or yield apparent strains for both FE analyses can be compared on Figure 3.14. For the fully brittle material behavior model, MID strains increase constantly with BV/TV as ultimate strains do. Both recurrence curves associated to these predicted values exhibit a very similar positive gradient, and possess p values equal or less than 0.0097, supporting their dependence with BV/TV. In opposition, for the fully ductile model, while yield strains increase with BV/TV, MID strains tend to decrease. Their associated recurrence curves display gradients with opposite signs, and p values beyond 0.0624, confirming their independence with BV/TV. To better interpret data on that figure, we calculate ratios between MID and ultimate or yield strains, for brittle and respectively ductile FE analyses (Figure 3.15).

As we could expect from Figure 3.14, we notice for the brittle material behavior model a constant ratio less than 1 because MID strains are always higher than ultimate strains, and their gradient are very similar. Since both ultimate and MID strains are dependent

on BV/TV, their corresponding ratio is thus independent to bone density (p value = 0.32).

On the other hand, for the ductile FEA, we point out that Yield/MID ratios tend to increase according to BV/TV. In other words, the higher the bone density the more apart the two strain values are. Since yield strains increase with BV/TV, we deduce that MID strains corresponding to local maximums on figure 3.13 is inversely proportional to BV/TV. These ratios are reliant on BV/TV (p value = 0.0003). For low-density specimens, the local maximum is situated at late steps (close to yield point). And for high density ones, that maximum is set at earlier steps (further from yield point).

To follow on from those results, we take into account the percentage of failed elements corresponding to both of these strain values (Figure 3.16). We notice that both ratios are absolutely not dependent on BV/TV. The fact that all ratios for the ductile FEA have approximately the same value can be explained as the following. For a low BV/TV specimen, after reaching the local maximum observed on figure 3.13, the percentage of failed elements decline with a very soft negative slope for another 1 or 2 additional steps until yield point. On the contrary, for a high BV/TV specimen, more elements fail in percentage of total amount. In order to obtain same ratio values, the percentage of incremental damage has to drop with a high negative slope after the maximum is reached and for longer (3-4 steps) because MID and yield strains are further apart.

3.6. *Imaging of Fracture Progression*

Concerning visualization of damage progression, we consider Figures 3.17-22. We observe for the specimen with the lowest BV/TV (Figure 3.17) that for the brittle model, tissues start to fail before 0.4% strain and damage proceed preferably in tension than compression. There is only a little amount of additional failed elements after 0.65% strain since the ultimate point has been reached and only a tiny amount of load is enough to break off the whole specimen. In the ductile model (Figure 3.18), failure also progress rather in tension than in compression but we can remark a nearly constant increase in failed tissue amount until 1% apparent strain. Regarding specimens with higher BV/TV (Figure 3.19, 3.21), there is almost no damage before 0.4% strain for brittle material behavior, and a tremendous failure increase between 0.55% and 0.65% strains. As the ultimate point is reached there is a smaller increase of failed elements. The specimen with highest BV/TV (Figure 3.21) contains more elements failing in

compression than in tension. There is a considerable amount of elements failing in tension located at the edges and extremities of trabeculae tissues. For these two specimens, considering tissue-level ductile material behavior (Figure 3.20, 3.22), we notice an approximately constant increase of failed elements along with the analysis. Consistently to figure 3.7, we observe a large quantity of elements failing during the last steps of the analysis, especially in a compressive fashion.

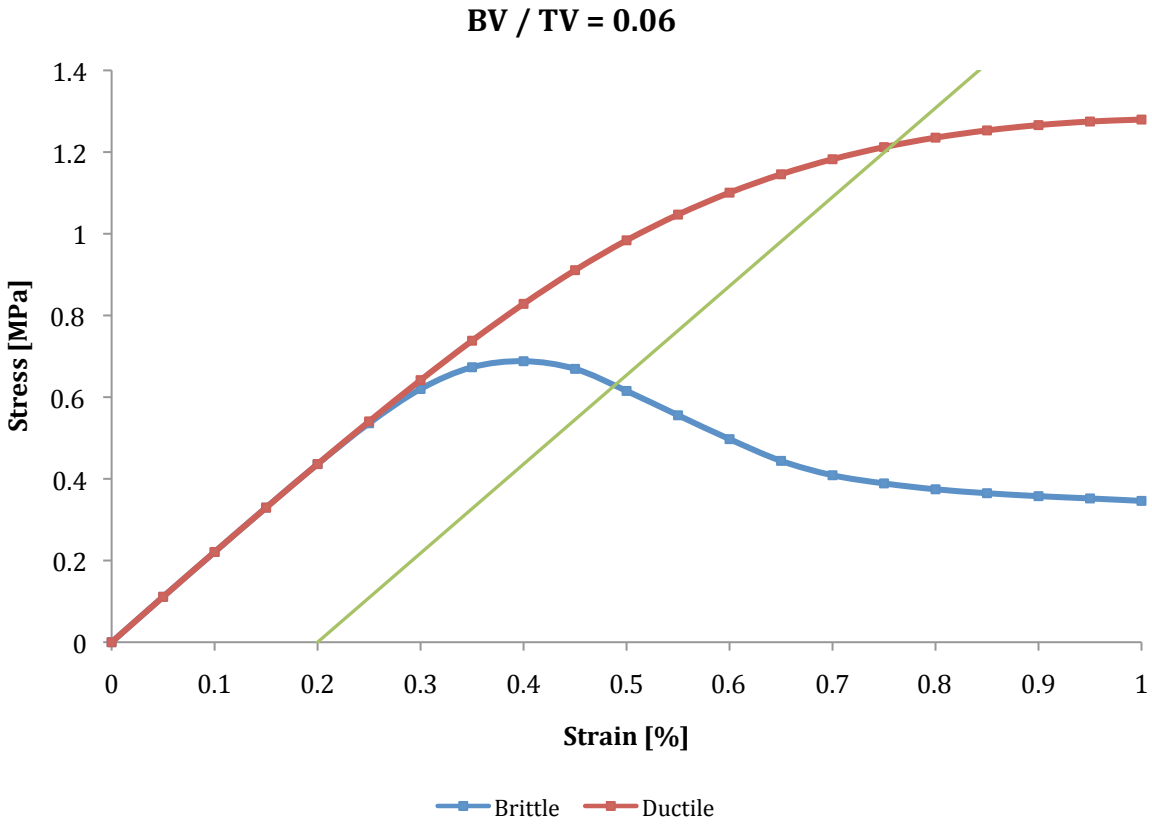
BV / TV = 0.06
Stress [MPa]
1.4
1.2
1
0.8
0.6
0.4
0.2
0
0
0.1
0.2
0.3
0.4
0.5
0.6
0.7
0.8
0.9
1
Strain [%]
Brittle
Ductile

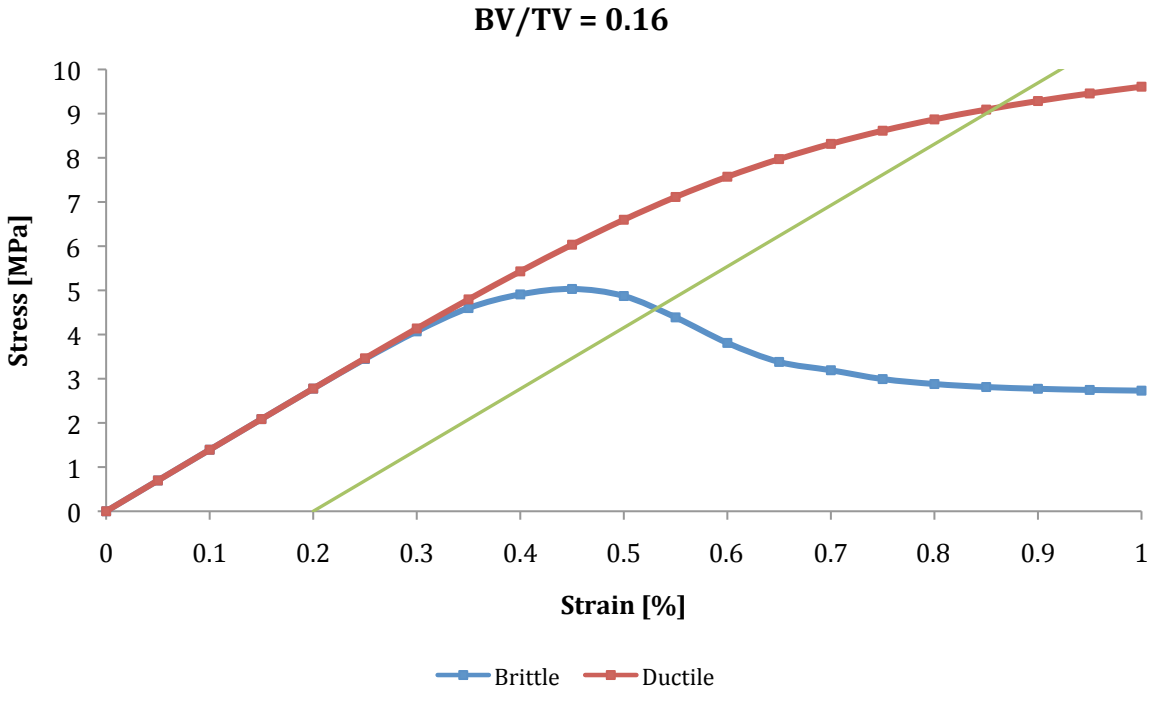
BV/TV = 0.16
Stress [MPa]
10
9
8
7
6
5
4
3
2
1
0
0
0.1
0.2
0.3
0.4
0.5
0.6
0.7
0.8
0.9
1
Strain [%]
Brittle
Ductile

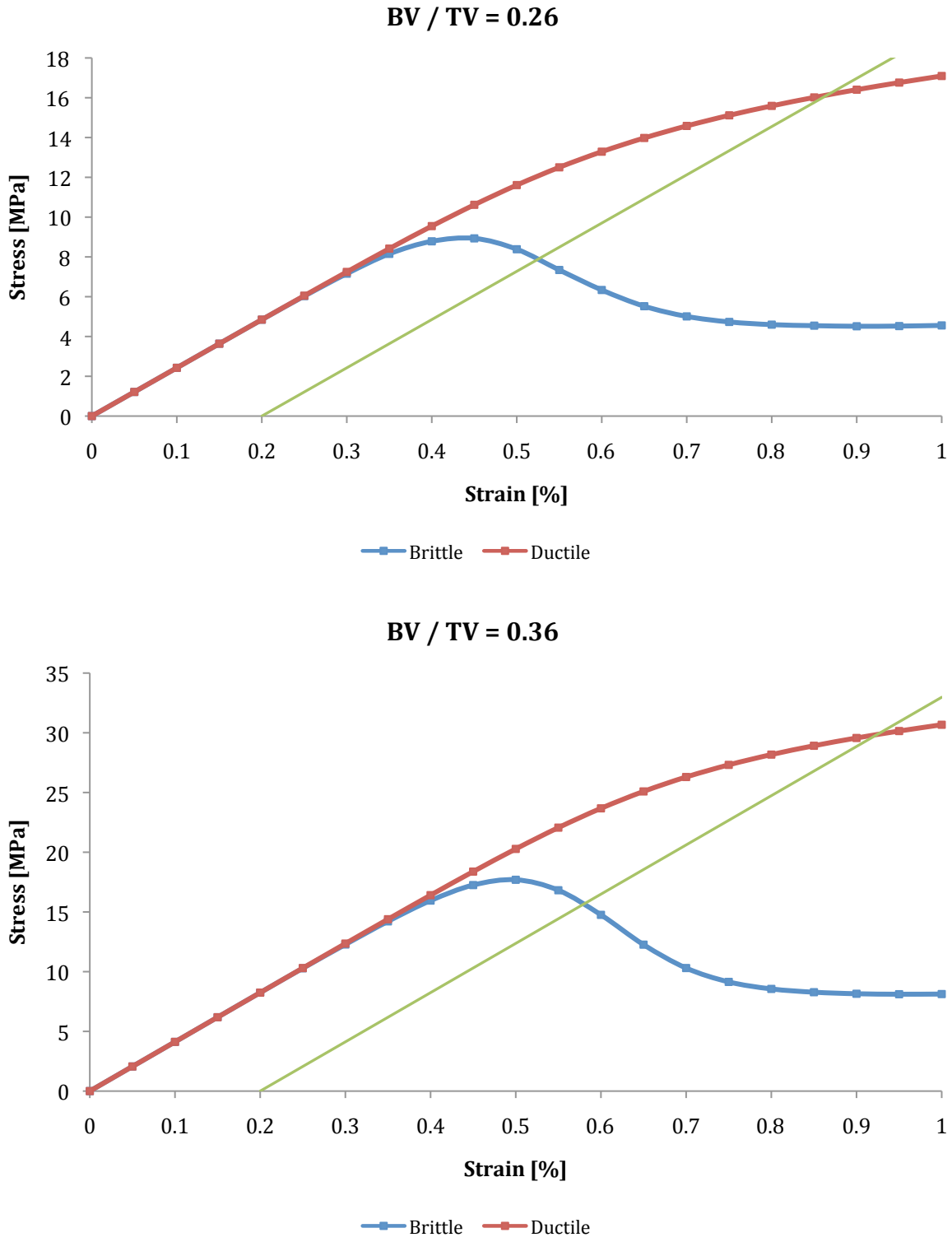

Figure 3.1. Compressive stress-strain curves at the apparent level for both brittle and ductile tissue-level material behavior FE analyses. Four specimens out of 21 are represented to give insight into the large range of densities.

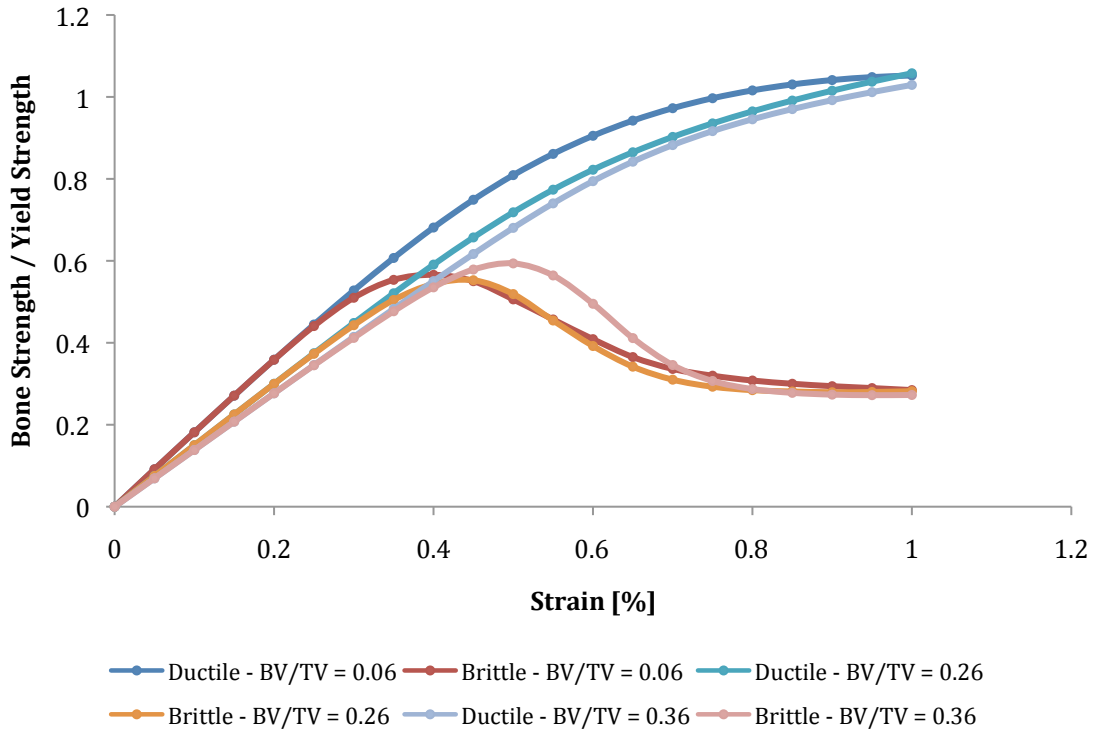

Figure 3.2. Apparent level compressive force-deformation curves for 3 specimens with different bone volume fraction. Strength values were modulated by the specimen yield strength obtained from ductile material behavior FEA.

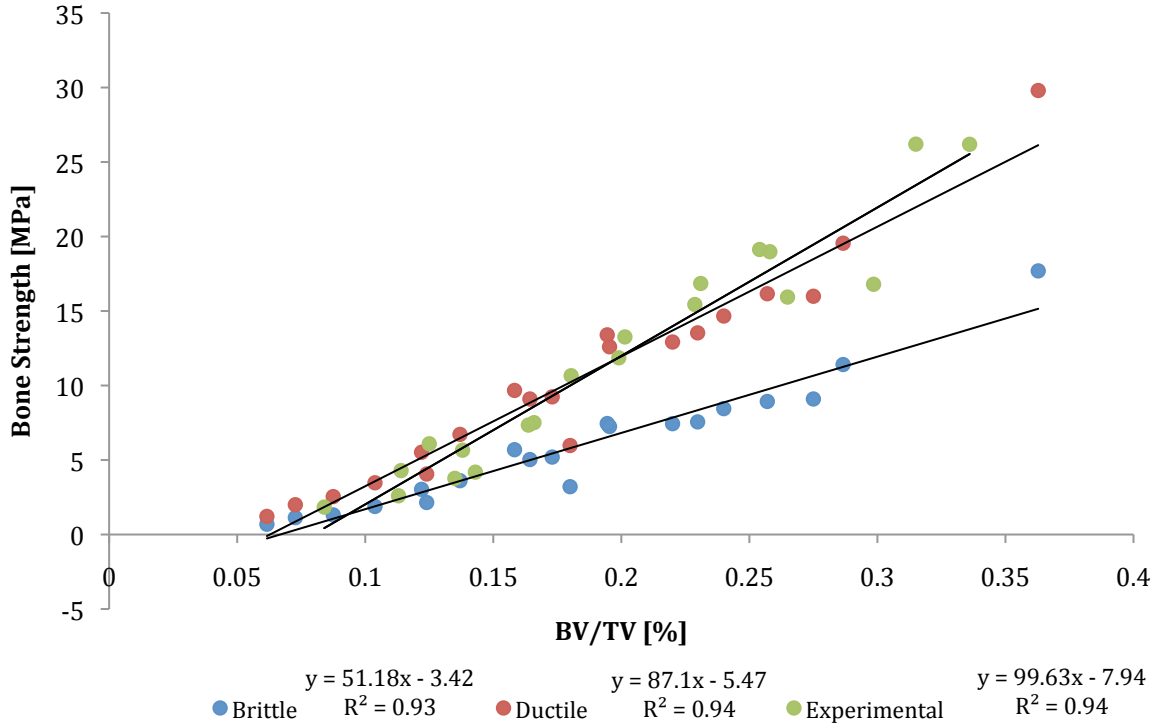

Figure 3.3. Ultimate stress obtained from brittle material behavior FEA vs. BV/TV. Yield stress vs. BV/TV ensues from experimental data, as well as from ductile material behavior FEA. Each dot stands for a unique specimen. Experimental data are gathered from different specimens than ours.Recurrence curves equations are mentioned, as well as their respective R^2.

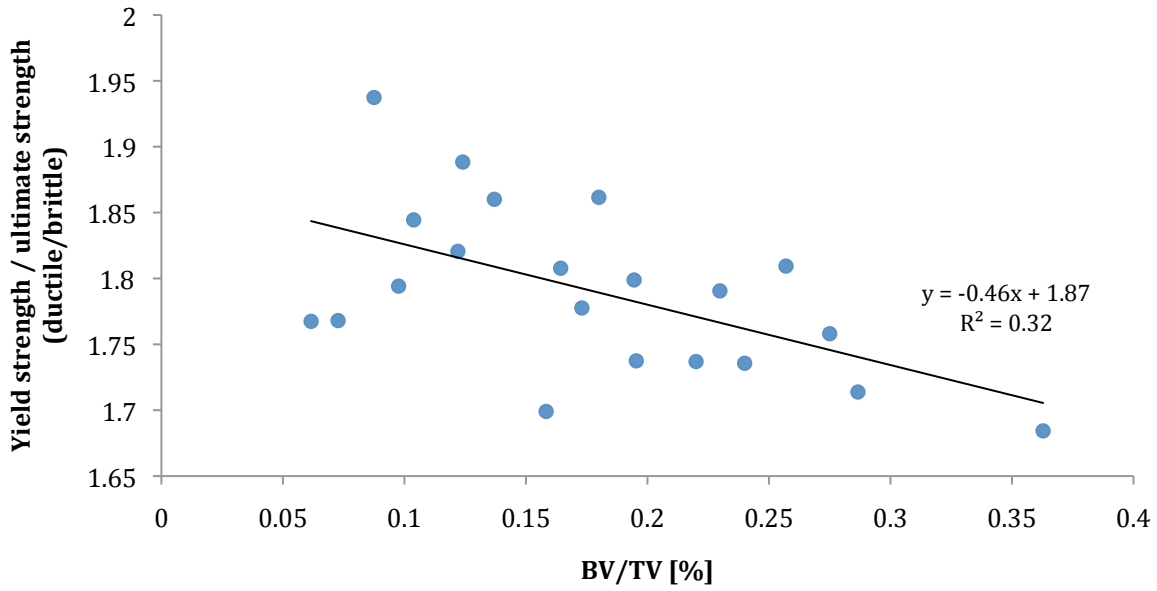

Figure 3.4. Strength ratios for each specimen obtained at yield point for ductile analysis, and at ultimate point for brittle analysis.

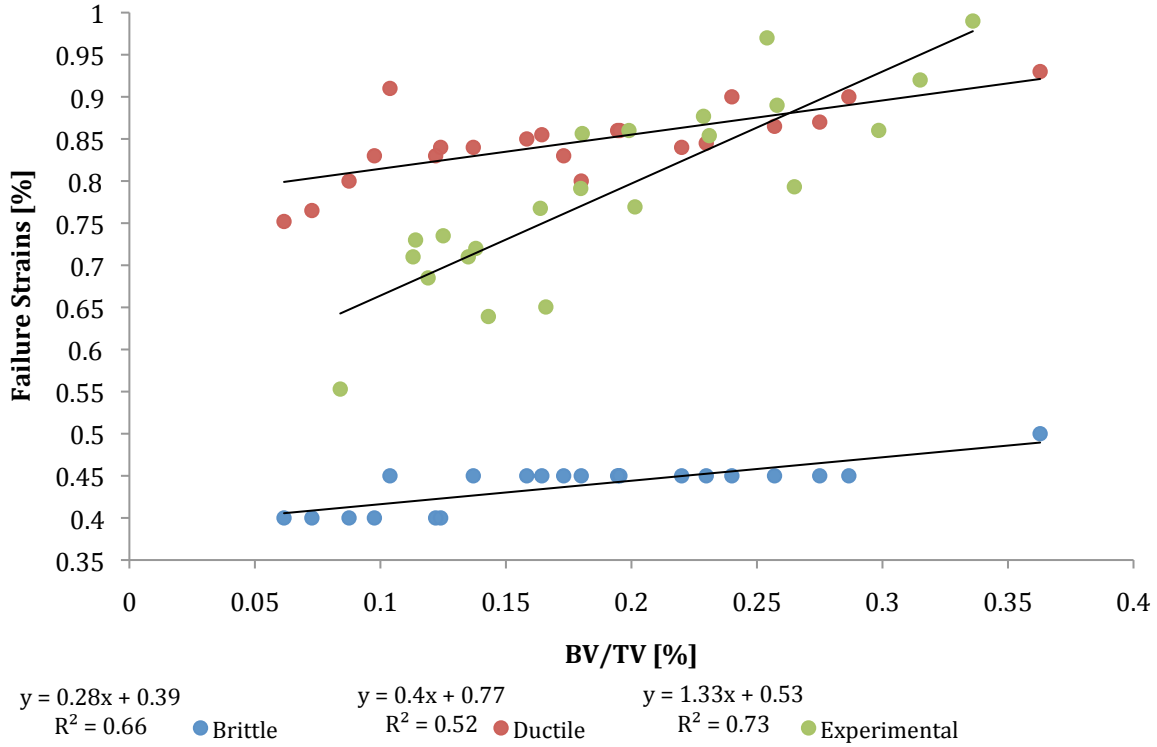

Figure 3.5. Strain values for each specimen gathered at ultimate point for brittle analysis, and at yield point for ductile analysis. Experimental strain values are collected at yield point and correspond to different specimens than ours.

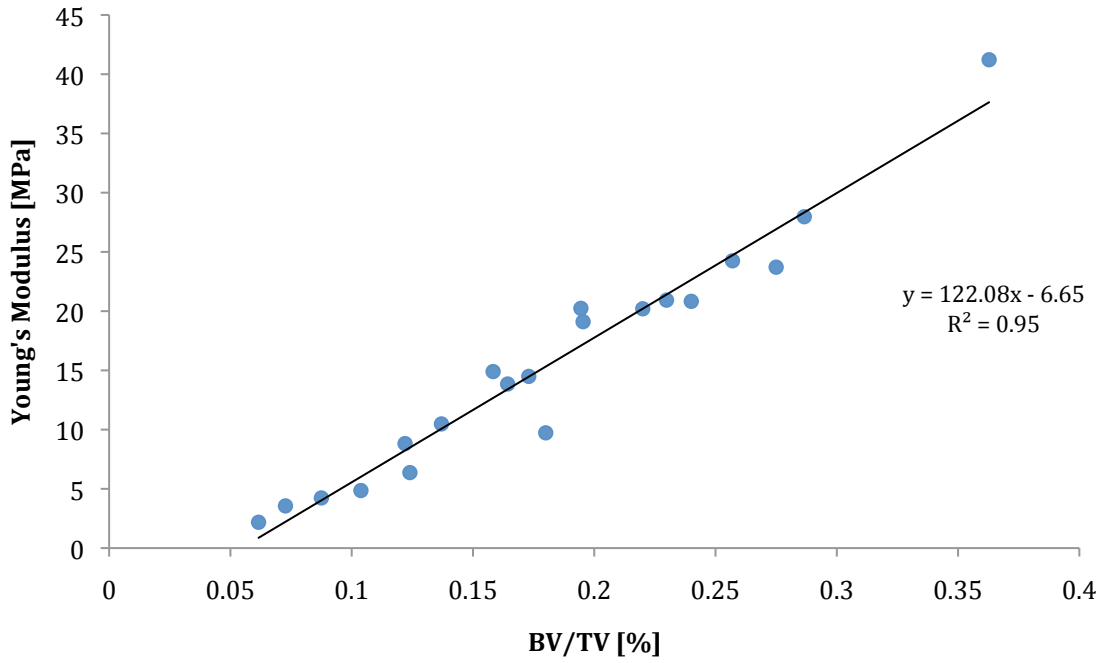

Figure 3.6. Young's Modulus of each specimen vs. BV/TV. Since both FE analyses adopt the same initial force-deformation curve, Young's Modulus data are the same for both of them.

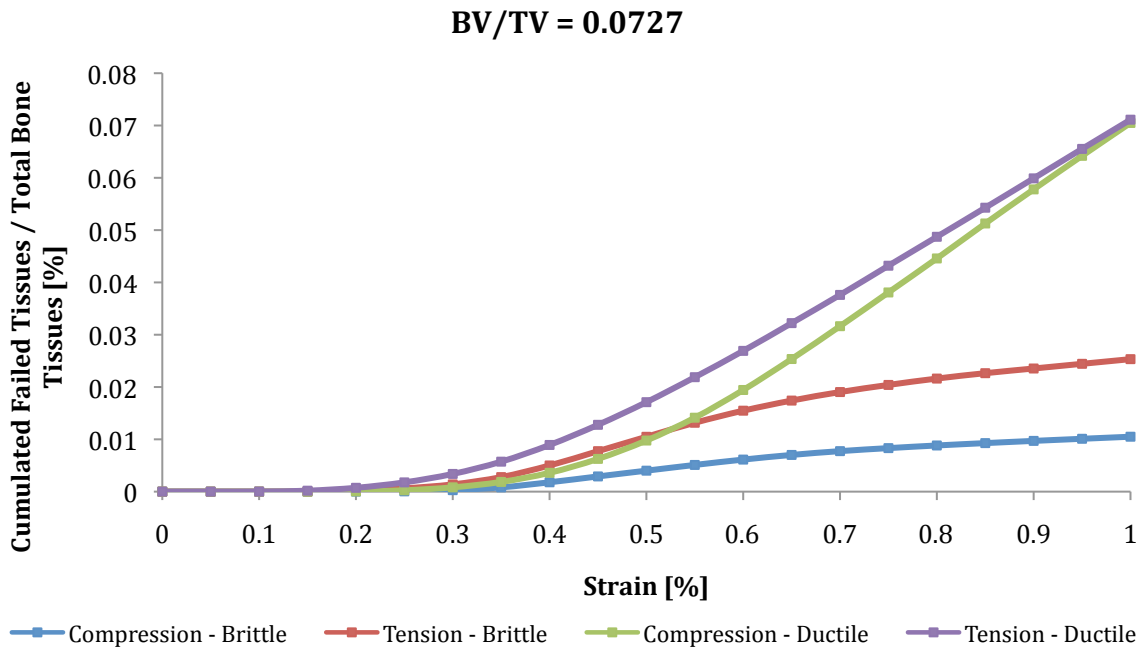

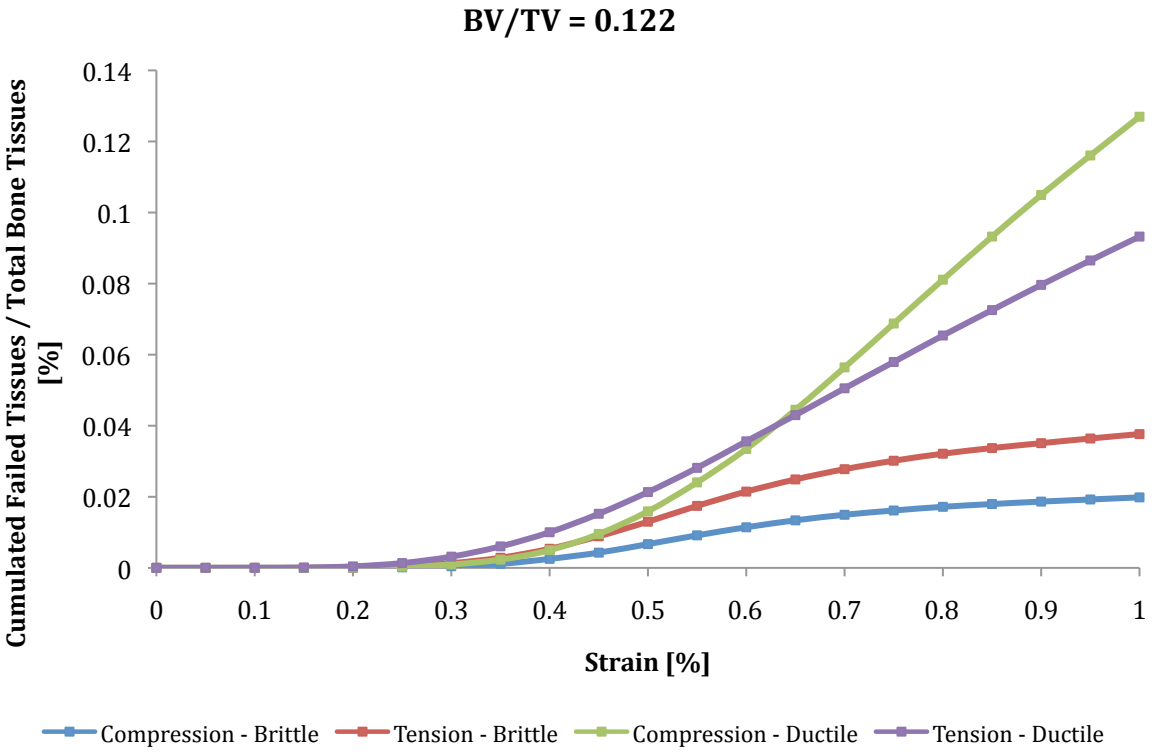
BV/TV = 0.122
Cumulated Failed Tissues / Total Bone Tissues [%]
0.14
0.12
0.1
0.08
0.06
0.04
0.02
0
0
0.1
0.2
0.3
0.4
0.5
0.6
0.7
0.8
0.9
1
Strain [%]
Compression - Brittle
Tension - Brittle
Compression - Ductile
Tension - Ductile

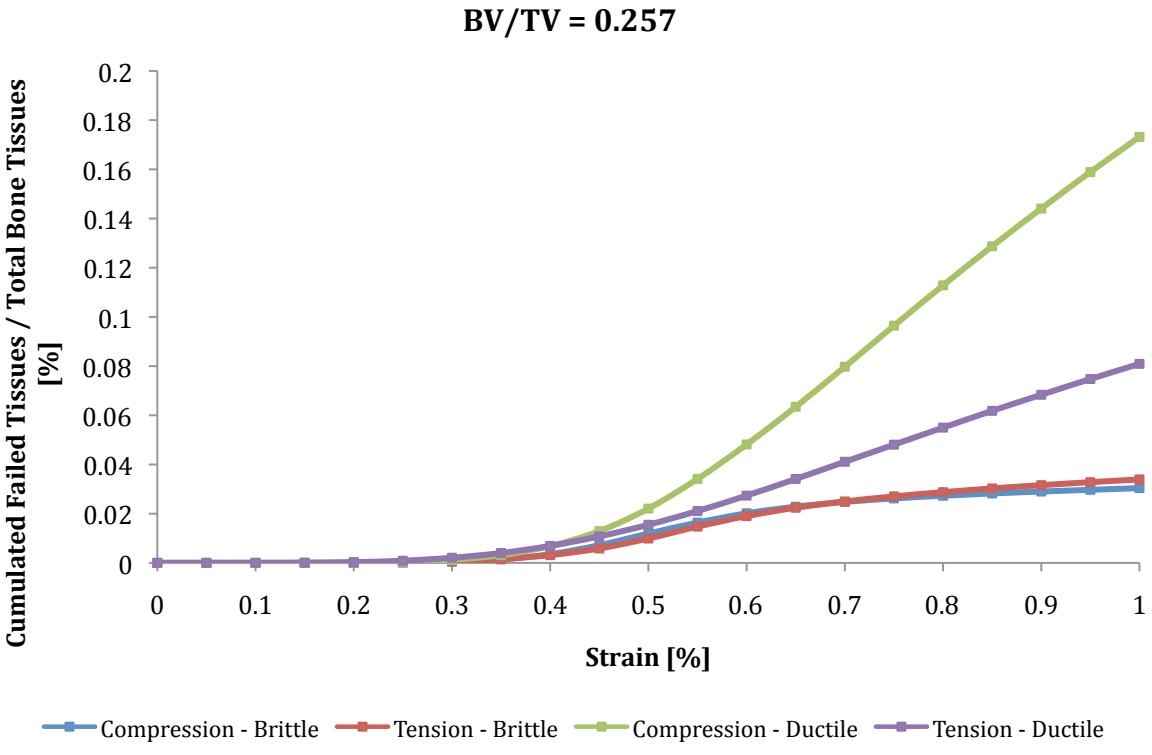
BV/TV = 0.257
Cumulated Failed Tissues / Total Bone Tissues [%]
0.2
0.18
0.16
0.14
0.12
0.1
0.08
0.06
0.04
0.02
0
0
0.1
0.2
0.3
0.4
0.5
0.6
0.7
0.8
0.9
1
Strain [%]
Compression - Brittle
Tension - Brittle
Compression - Ductile
Tension - Ductile

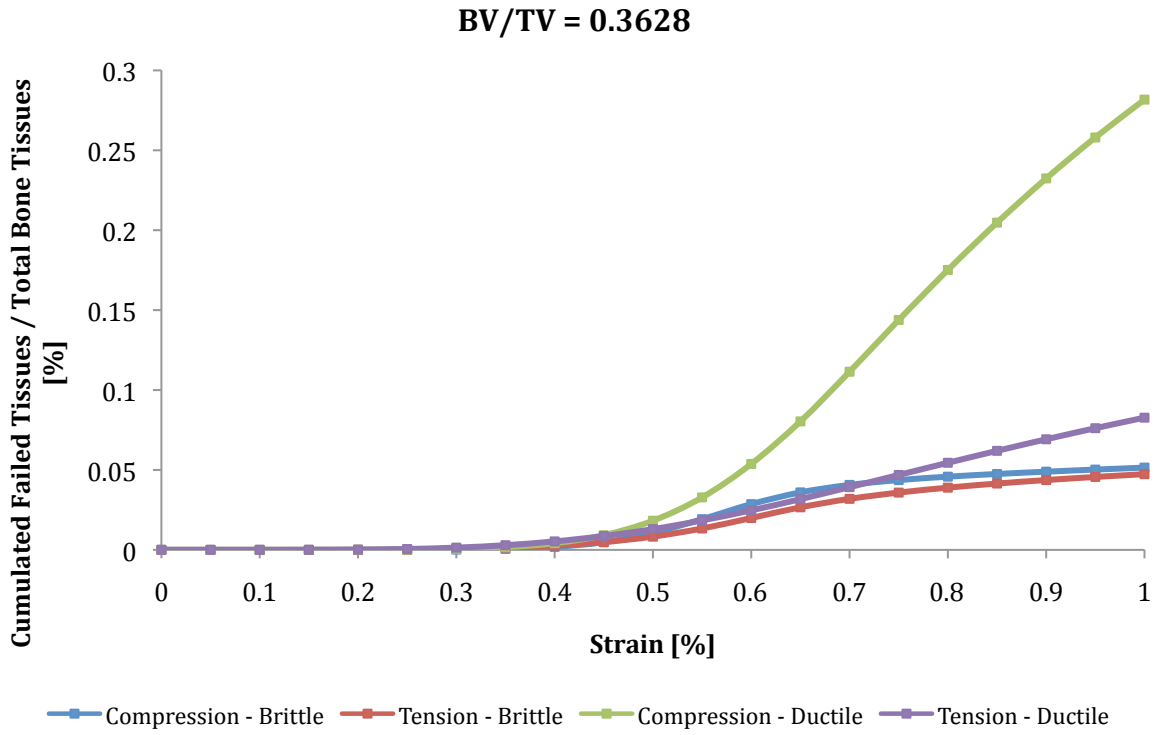

Figure 3.7. Cumulative percentage of failed tissues in compression and tension for 4 specimens with different BV/TV.

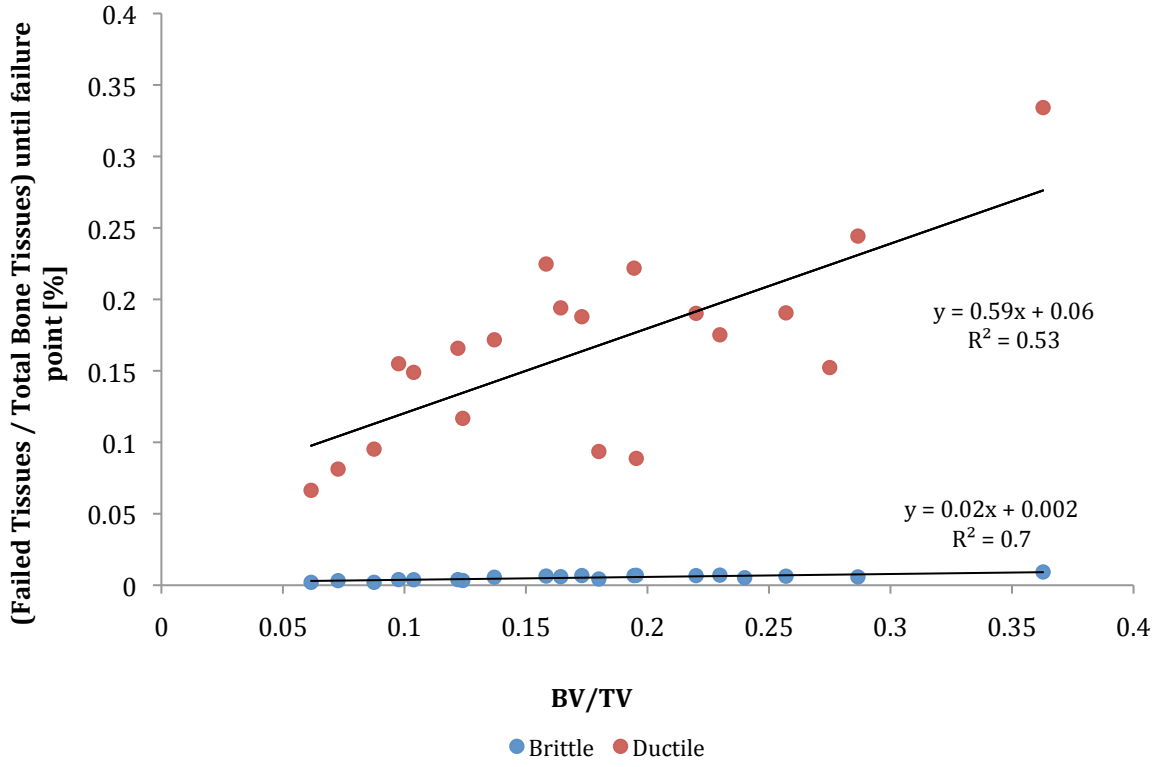

Figure 3.8. Cumulative percentage of failed tissues in tension and compression until failure point vs. BV/TV

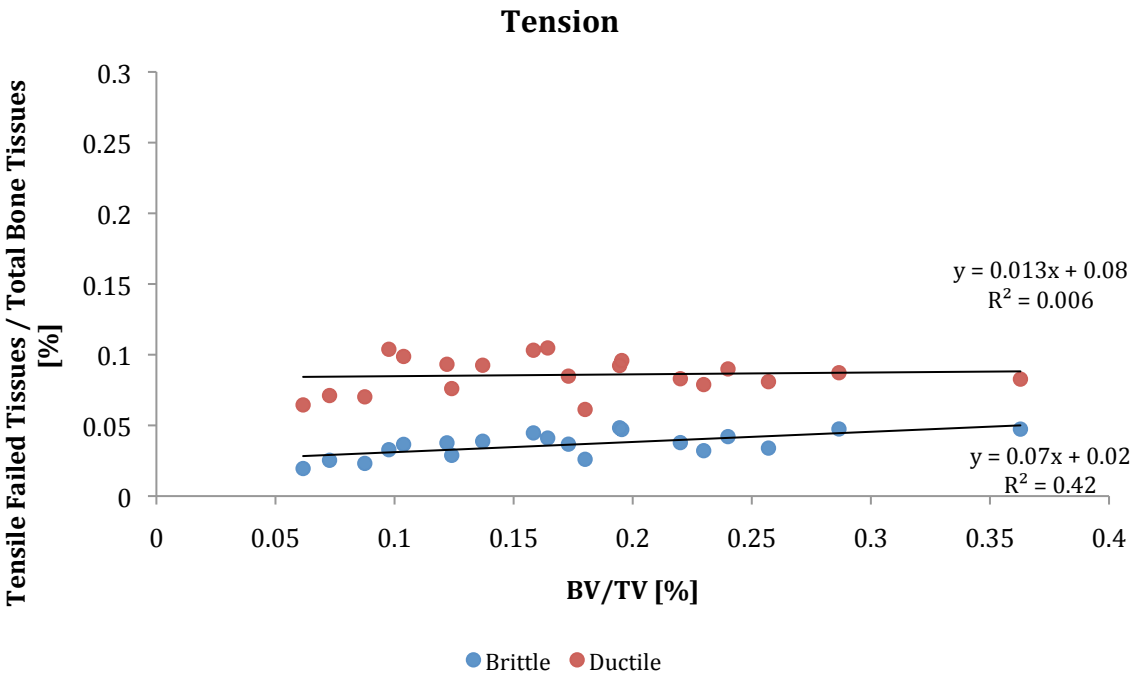

Figure 3.9. Cumulative percentage of failed tissues in Tension until 1% apparent strain vs. BV/TV.

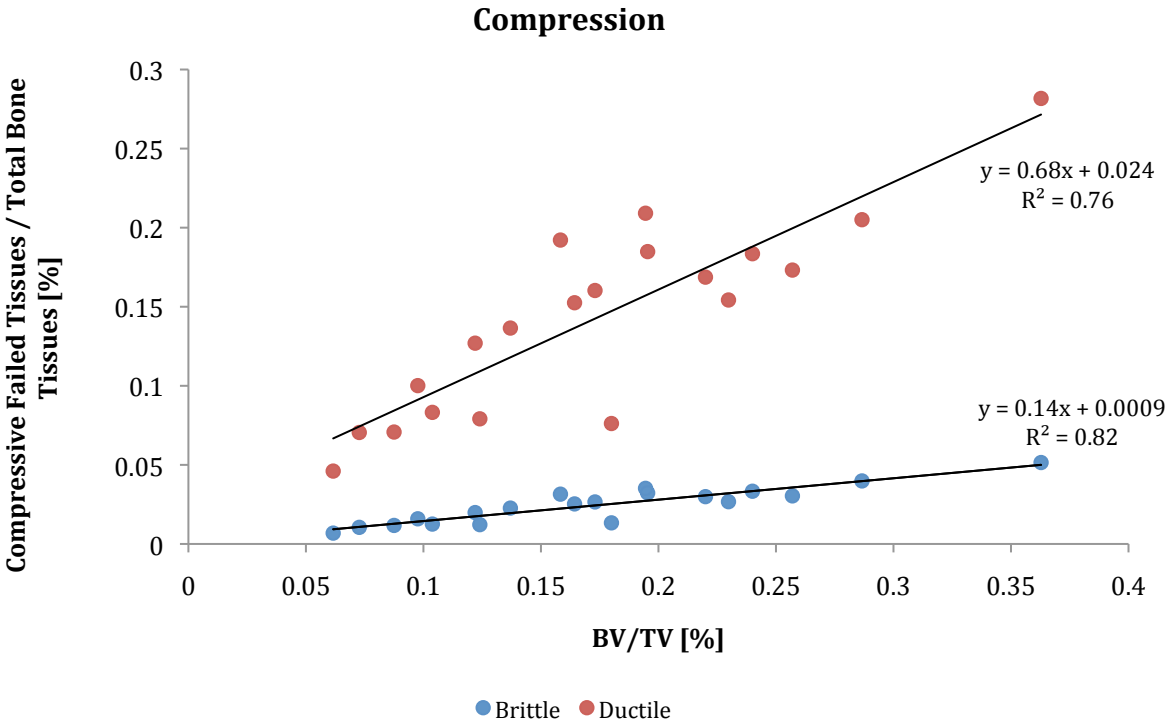

Figure 3.10. Cumulative percentage of failed tissues in Compression until 1% apparent strain vs. BV/TV.

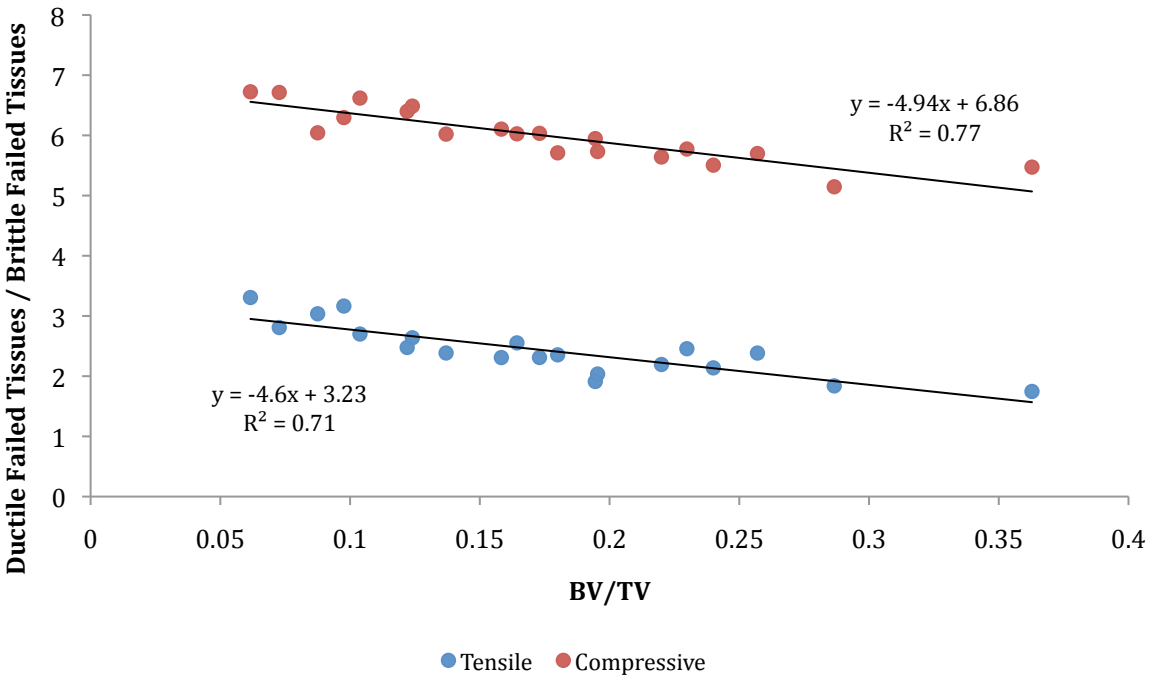

Figure 3.11. Ratios between ductile and brittle FEA predicted amounts of failed tissues in tension and compression vs. BV/TV.

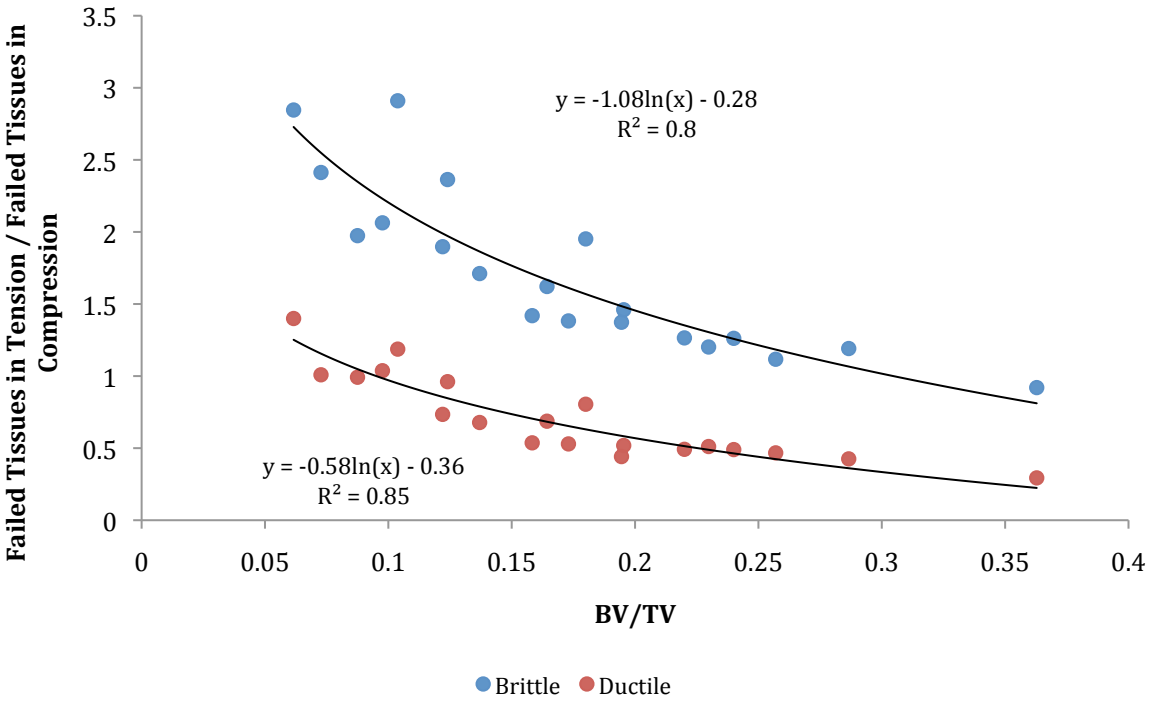

Figure 3.12. Ratios between tensile and compressive total amount of failed tissues vs. BV/TV for both perfectly ductile, and brittle FEA.

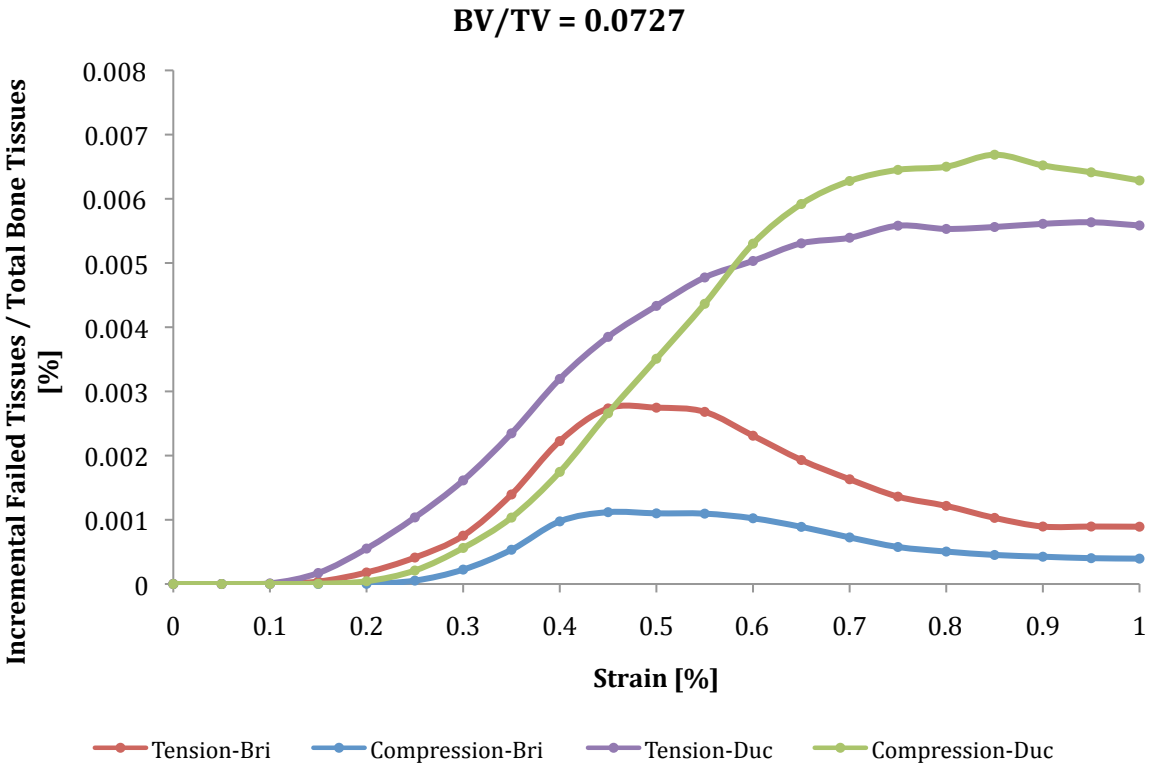
BV/TV = 0.0727
Incremental Failed Tissues / Total Bone Tissues [%]
0.008
0.007
0.006
0.005
0.004
0.003
0.002
0.001
0
0
0.1
0.2
0.3
0.4
0.5
0.6
0.7
0.8
0.9
1
Strain [%]
Tension-Bri
Compression-Bri
Tension-Duc
Compression-Duc

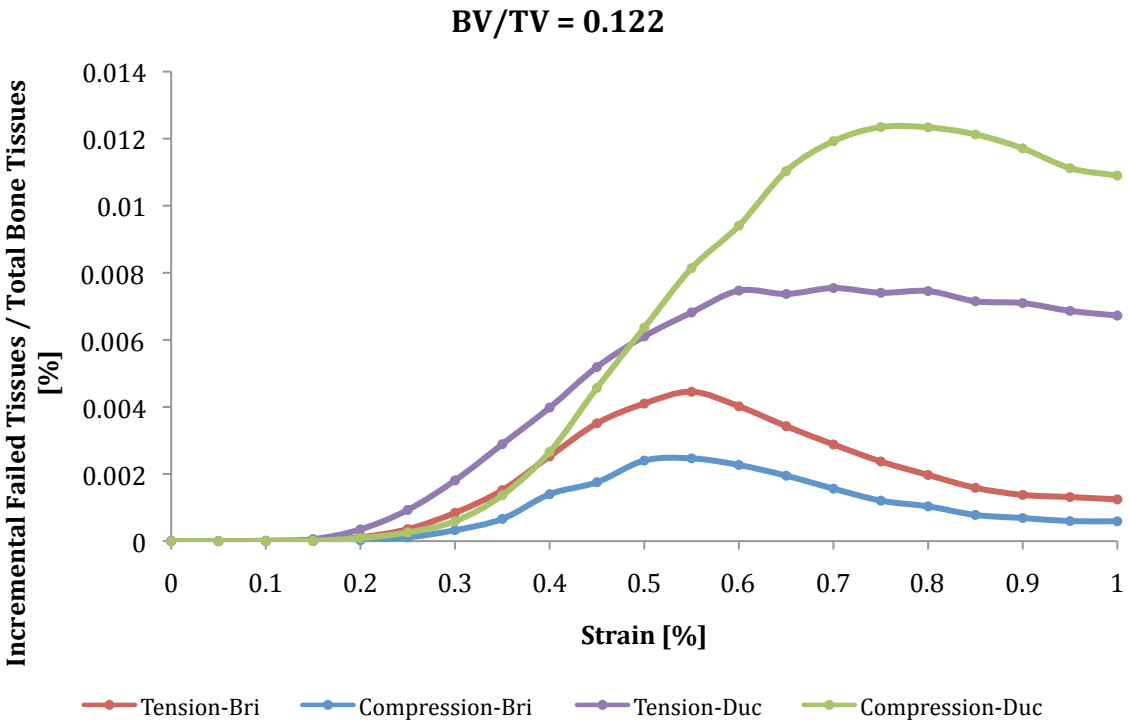
BV/TV = 0.122
Incremental Failed Tissues / Total Bone Tissues [%]
0.014
0.012
0.01
0.008
0.006
0.004
0.002
0
0
0.1
0.2
0.3
0.4
0.5
0.6
0.7
0.8
0.9
1
Strain [%]
Tension-Bri
Compression-Bri
Tension-Duc
Compression-Duc

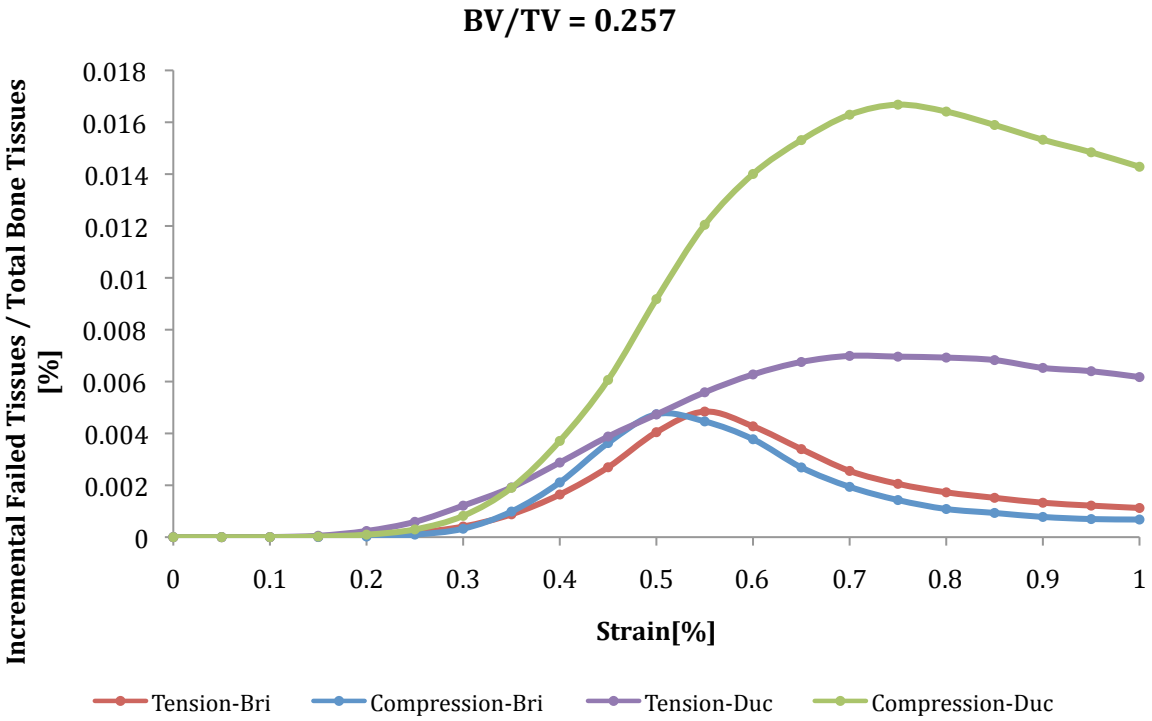

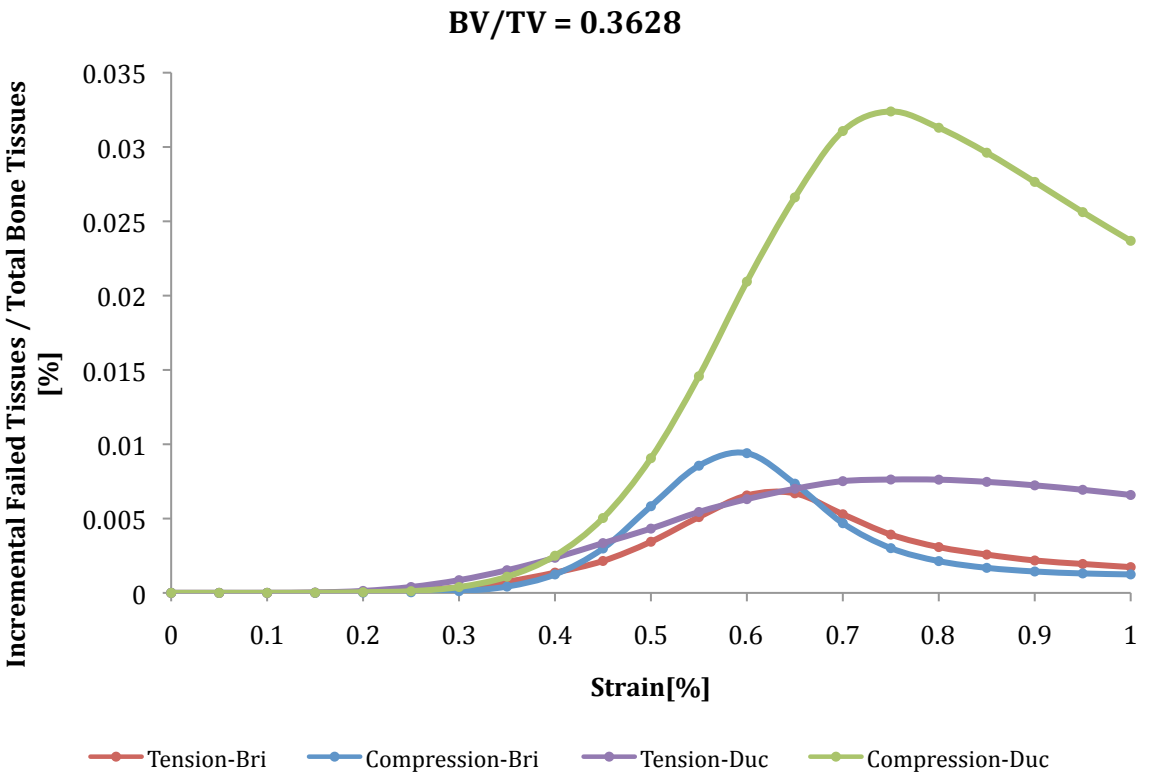

Figure 3.13. Incremental damage (tension and compression) in percentage of failed tissues at each step, for both perfectly ductile and brittle FEA.

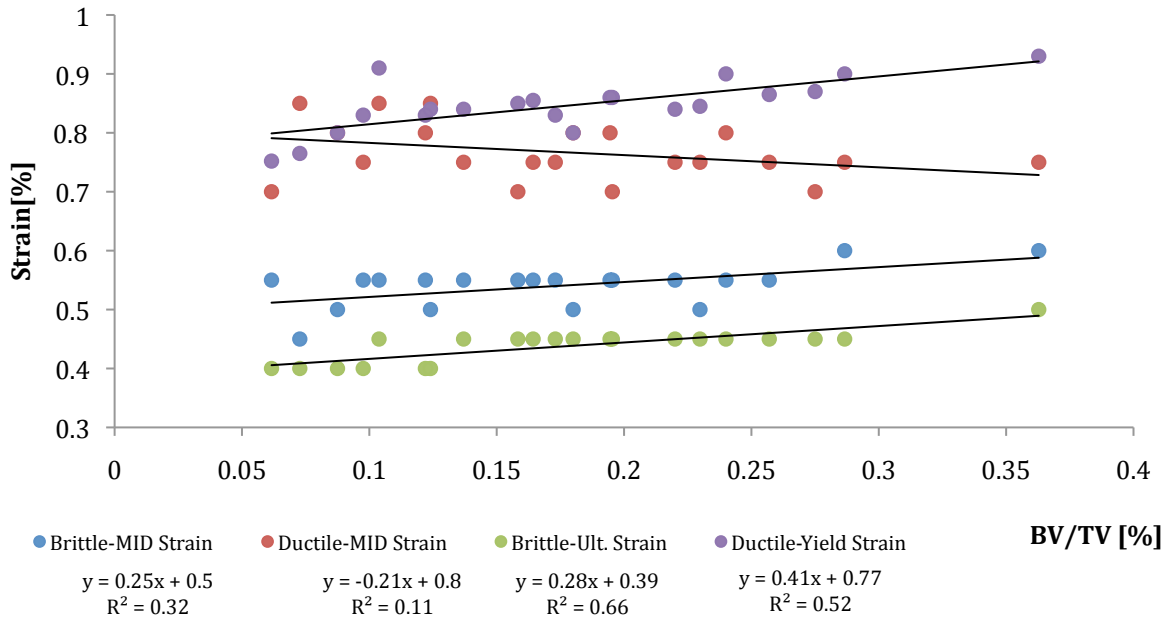

Figure 3.14. "Maximal Incremental Damage" strain values, as well as ultimate or yield strain predicted data for respectively perfectly brittle and perfectly ductile FEA, for the whole range of specimens.

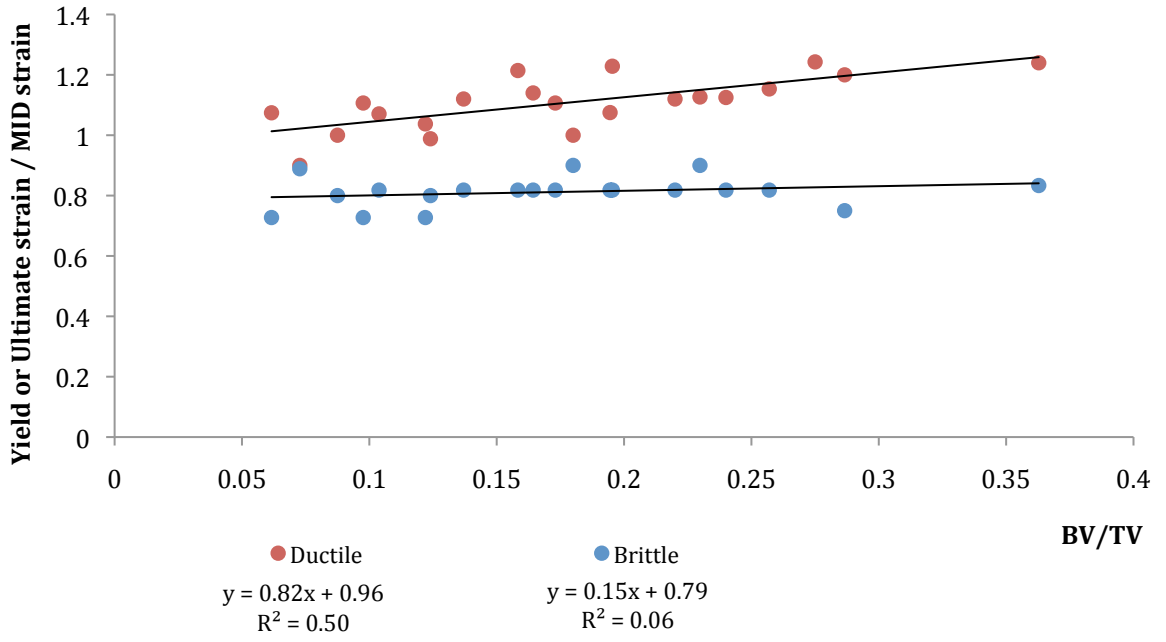

Figure 3.15. Ratios between ultimate or yield strain predicted values and MID strains vs. BV/TV, for respectively perfectly brittle or ductile FEA.

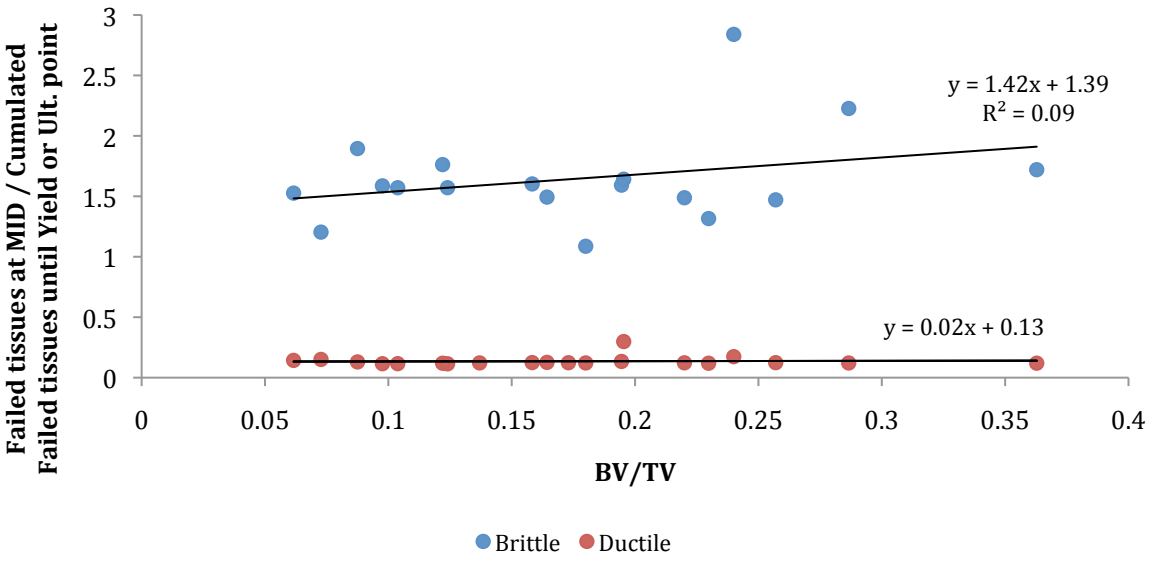

Figure 3.16. Ratio between failed elements at MID and cumulated failed elements until yield or ultimate point vs. BV/TV.

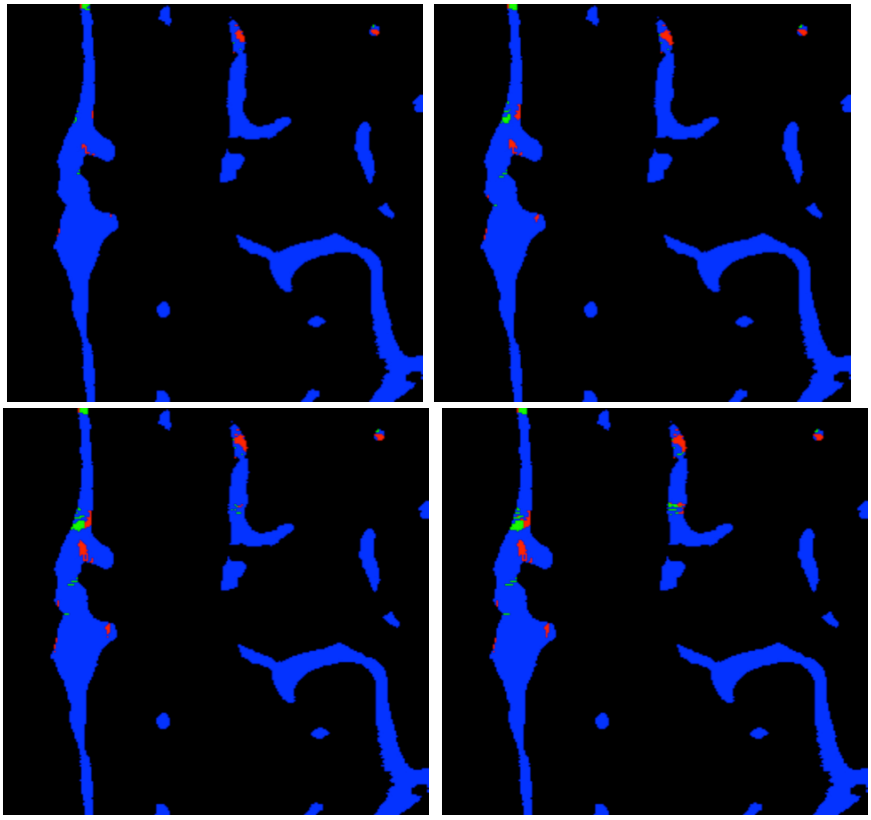

Figure 3.17. Outputs from a perfectly brittle quasi-nonlinear FE analysis of trabecular bone (BV/TV = 0.06; 20-micron element size). Thin slices (from top left to bottom right: 0.45, 0.55, 0.65, and 1% compressive load) showing the cumulative distribution of fractured tissue in tension (red) and compression (green). The second and third images, being in the midst of structural collapse, best identify the weak-link locations.

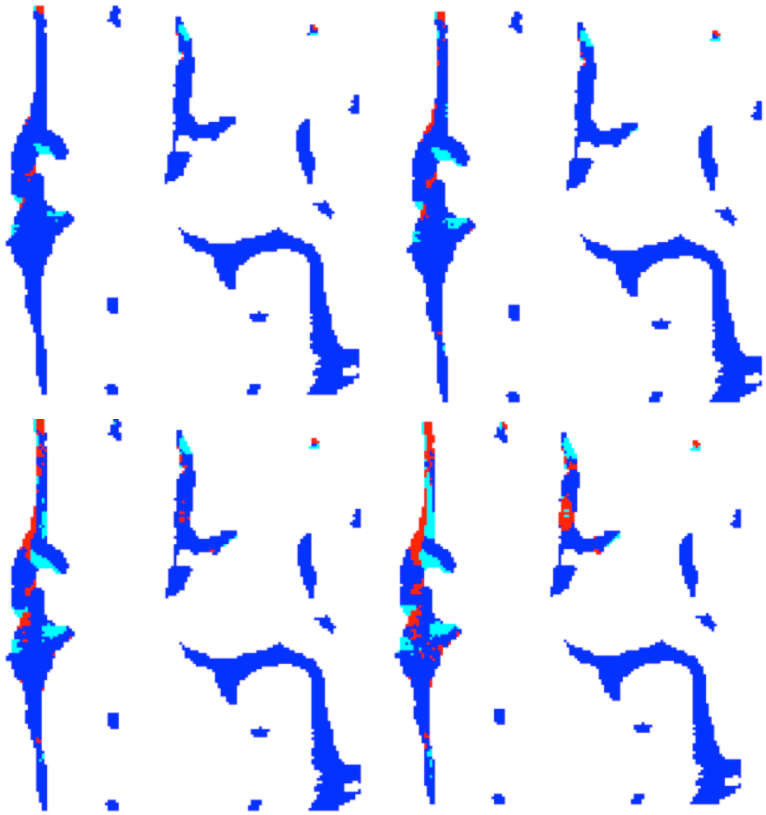

Figure 3.18. Outputs from a perfectly ductile quasi-nonlinear FE analysis of trabecular bone (BV/TV = 0.06; 20-micron element size). Thin slices (from top left to bottom right: 0.45, 0.55, 0.65, and 1% compressive load) showing the cumulative distribution of fractured tissue in tension (red) and compression (green).

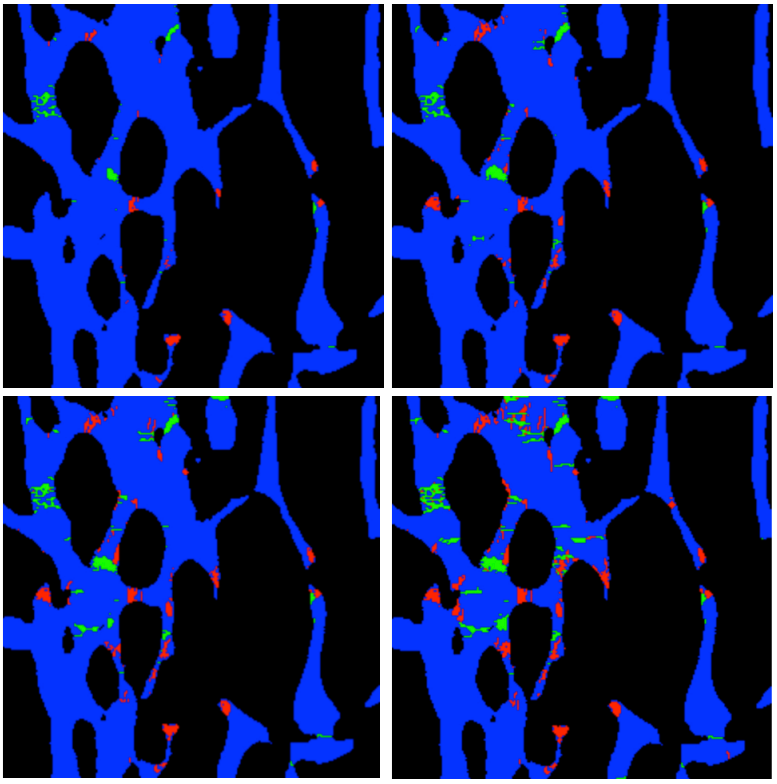

Figure 3.19. Outputs from a perfectly brittle quasi-nonlinear FE analysis of trabecular bone (BV/TV = 0.22; 22-micron element size). Thin slices (from top left to bottom right: 0.45, 0.55, 0.65, and 1% compressive load) showing the cumulative distribution of fractured tissue in tension (red) and compression (green). The second and third images, being in the midst of structural collapse, best identify the weak-link locations.

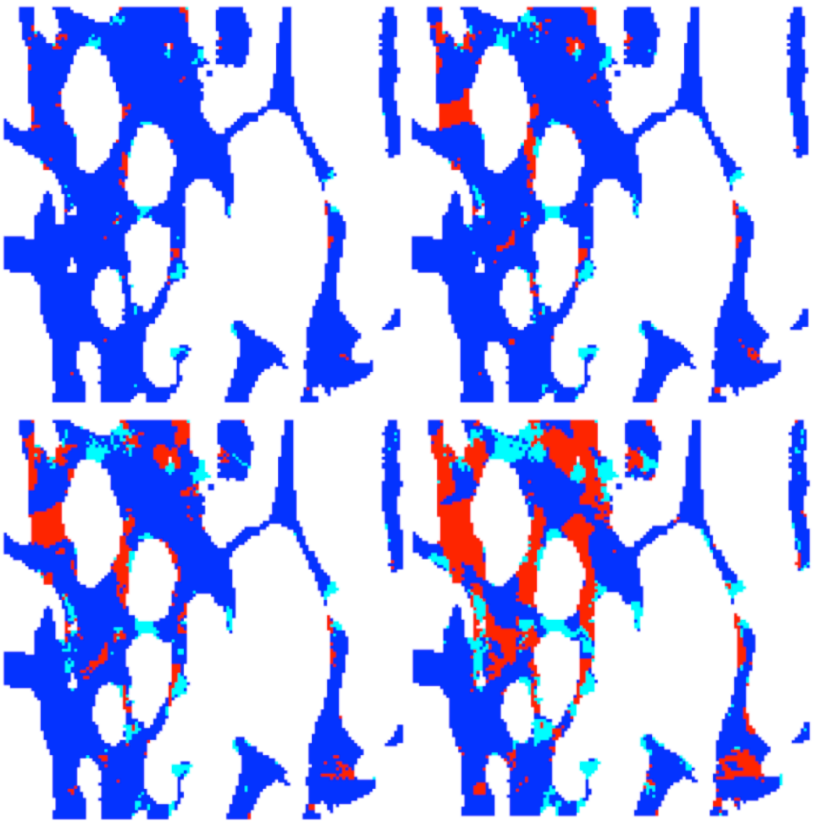

Figure 3.20. Outputs from a perfectly brittle quasi-nonlinear FE analysis of trabecular bone (BV/TV = 0.06; 20-micron element size). Thin slices (from top left to bottom right: 0.45, 0.55, 0.65, and 1% compressive load) showing the cumulative distribution of fractured tissue in tension (red) and compression (green). The second and third images, being in the midst of structural collapse, best identify the weak-link locations.

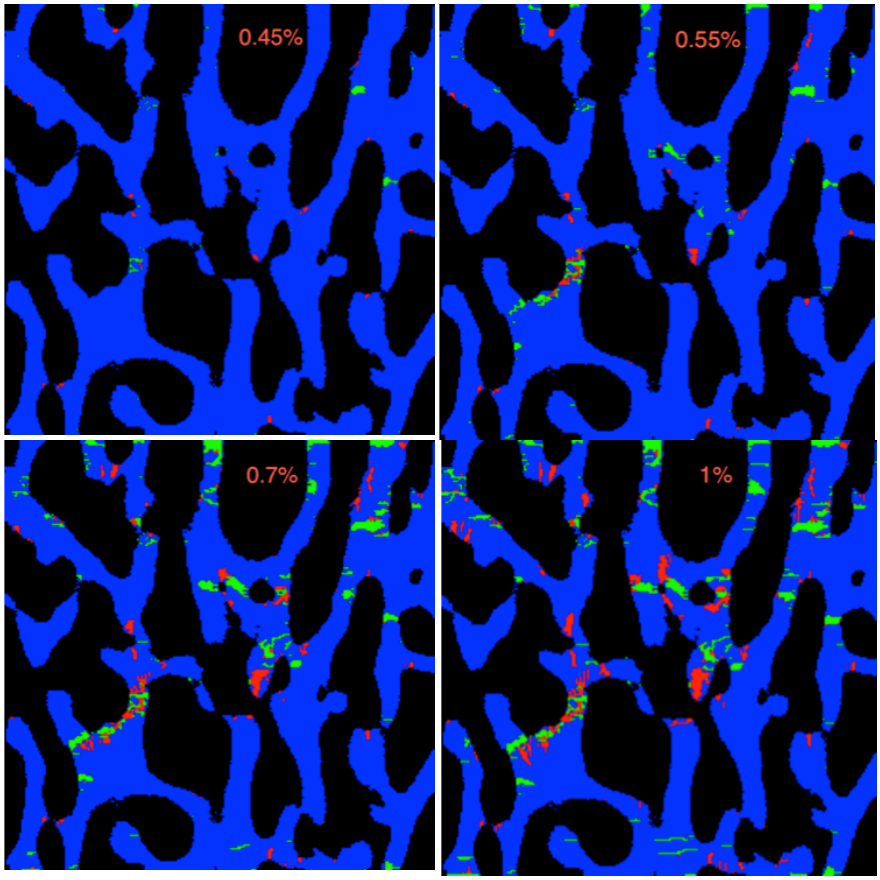

Figure 3.21. Outputs from a perfectly brittle quasi-nonlinear FE analysis of trabecular bone (BV/TV = 0.36; 20-micron element size). Thin slices (from top left to bottom right: 0.45, 0.55, 0.7, and 1% compressive load) showing the cumulative distribution of fractured tissue in tension (red) and compression (green). The second and third images, being in the midst of structural collapse, best identify the weak-link locations.

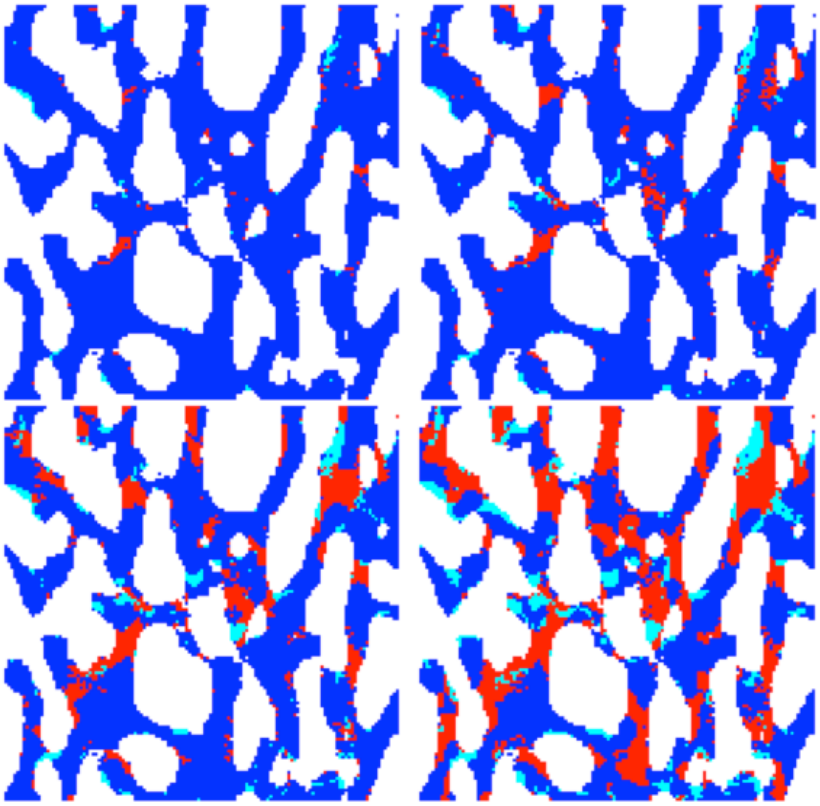

Figure 3.22. Outputs from a perfectly brittle quasi-nonlinear FE analysis of trabecular bone (BV/TV = 0.36; 20-micron element size). Thin slices (from top left to bottom right: 0.45, 0.55, 0.7, and 1% compressive load) showing the cumulative distribution of fractured tissue in tension (red) and compression (green).

4. DISCUSSION

The goal of this study was to develop numerical analyses that model perfectly brittle and perfectly ductile tissue-level material behavior of spongy bone samples. We sought to compare ductile and brittle analyses to identify weak-link regions of trabecular cubes. By contrasting the structural responses of the two types of the nonlinear analyses, we can bracket the bounds of overall structural behavior associated with these extremes of post-yield tissue behavior (perfectly ductile vs. perfectly brittle) and thus gain unique insight into the structural effects of post-yield behavior.

The first outcome studied was the strength at the apparent level obtained for these two finite element analyses. We assume that bone volume fraction can account for much of the variations in trabecular strength for both FE analyses. The force-deformation curve for the whole structure for the fully brittle analysis reveals a clearly defined ultimate point, after which the curve drops rapidly (Figure 3.1, 3.2). If additional load is applied on the whole specimen, the latter will completely collapse. Thus, only a tiny amount of elements can fail before the whole specimen collapse, indicating a very small redundancy of the specimen.

We concluded from figure 3.3 that the overall trabecular strength can vary two-fold if the tissue is entirely brittle compared to entirely ductile. This is a huge effect, and it appears to be independent of bone volume fraction. We detect however a bigger effect for low bone density specimens because they are mostly made of rod-like structures, which are more able to fail in tension when the tissue bends under compressive load than higher BV/TV specimens, mainly composed of plate-like structural tissues. Consequently, this gives us the confirmation that large deformation has more repercussions in brittle than ductile tissues in low BV/TV specimens.

The recurrence curve affiliated to the plot of apparent strength obtained with brittle vs. ductile models shows the dependence between these two parameters. According to this high reliance, it is thus possible to predict strength values of the brittle model with the ductile one, and vice-versa (Figure 4.1).

Comparison of the model predictions against the experimental data confirmed that the model provided a bound on real behavior (figure 3.5). These observations suggest that

any variations in real tissue ductility may be unimportant at high bone volume fraction since the real behavior mimics that of perfectly ductile behavior. But at low bone volume fraction, real variations in tissue ductility could be more important since the real behavior falls between the ductile and brittle behaviors. If so, this implies that future studies assessing the structural consequence of changes in tissue-level ductility need to consider the bone volume fraction. However, we must stay aware that strain values for the brittle analysis were deduced from local maximum on figure 1, which may only appear at a particular step, therefore, those values can exclusively be a multiple of 0.05, displaying a reduced accuracy.
Both models possess the same Young's Modulus. Figure 3.6 confirms observations presented in the literature [1] by denoting the highly dependence between Young's modulus and BV/TV (p value < 0.0001).

Considering the percentage of failed elements (figure 3.7), we noticed for the brittle model more elements failing under tension across the range of densities, in opposition to the ductile analysis. However more elements fail under compression in the specimen with highest BV/TV, confirming that fewer tissues bend (less large deformation repercussion). Since tissue-level tensile yield strain is lesser than the compressive one, we can detect large deformation effects for both FE models on figure 3.13, where a considerable amount of tissue fail initially in tension, demonstrating that tissues bend. It is also possible to visualize that large-deformation effect on the lowest BV/TV specimen (Figure 3.17). We remark that elements fail in tension on the right side of the top-left trabeculae and in a compressive way on the other side. There are nearly no additional failed elements after 0.65% strain in this region since the whole tissue presumably collapsed.

Brittle material behavior model predict much less elements to fail (Figure 3.8). This might be explained by the fact that data linked to ultimate points are gathered at very low strains. Additionally, the slope of the brittle recurrence curve (Figure 3.8) is far lower than the ductile one, which can be explained by the exponential behavior attributed to compressive and tensile amounts of failed elements in the ductile model.

We noticed that the ductile model always predicted more elements to fail than the brittle model, for the whole range of specimens. We thus believe that the brittle model is more sensitive to bone density since the load path is contracted as the specimen fails.
With BV/TV increases, tensile over compressive ratios of total number of failed tissues decrease in both analyses (Figure 3.12), indicating that more and more tissues fail in compression, while tensile values remain rather constant. However, since brittle FE analysis predicts tensile and compressive failed elements amounts closer to ductile ones as BV/TV increases, we consider that geometry effects are more important than material behavior impact.

We observed for the brittle model that MID (maximum incremental damage) strains are always higher than ultimate strains (demonstrating a constant ratio between these two parameters), and their recurrence curves gradients are very similar. However, considering the ductile model, yield/MID apparent strain ratios tend to increase according to BV/TV (Figure 3.15). Since predicted yield strains increase with BV/TV, we deduce that MID strains are inversely proportional to BV/TV (Figure 3.14). We can presume that a specimen with high bone volume fraction has so many elements that even after reaching its maximal failure step it still can afford to keep deforming and loosing new elements until it yields at the apparent level. On the other hand, when a specimen with very low bone density reaches its maximal damage step, there remains a smaller amount of element to support the overall load and thus it will yield very soon.

We investigated specimens' toughness prior to the fracture for both models (appendix 5.3) by calculating areas under apparent-level stress-strain curves until failure point. In the same way at bone strength, toughness is highly dependent on bone volume fraction. Moreover, we recorded a mean ratio between ductile and brittle toughness approaching 3.5. Since the mean ratio between ductile and brittle bone strength is equal to 1.79, we assume that the mean ratio between toughness and strength is approximately 2. The same conclusion has already been demonstrated [46].

One of the novelties of this study was the application of high-resolution finite element modeling to a large sample size of human trabecular bone taken from a range of anatomic sites that displayed wide variations in bone volume fraction [3]. Since the

computer models used here only included variations in bone volume fraction and tissue-level material properties between specimens, our results indicate that there exists a bone quality effect related to tissue behavior that can be very large in low-density specimens. For now, since experimental measures cannot predict the biomechanical effects of post-yield tissue behavior, utilization of fully nonlinear finite element analysis on micro-CT scans of trabecular bone may provide unique insight into bone quality effects [3]. Advances in computational resources and highly scalable parallel finite element code [43] enabled us to process a large number of specimens efficiently, although it is expected that such analyses will soon become more routine as computational resources continue to expand [33].

Although the overall robustness of the techniques used in this study, certain weaknesses should also be pointed out. Foremost, in order to address mechanical properties at a particular size scale, samples should be selected with decent physical proportions. A recent study stipulate that specimens smaller than 4-5 mm are not sufficiently large to explicitly interpret the trabecular structure and thus do not satisfy the continuum assumption [44]. Accordingly, since the specimens we used are 5mm edge cubes, their dimensions are set at the limit of the accepted structure size. It may be interesting to extend our research in the future with larger specimens, and we would expect to obtain predicted results of percentage of failed tissues shifted up (Figure 3.8).
We should stay aware that we compared our results (gathered from cubic 3D models) with experimental results made out of cylindrical specimens.

Secondly, the sample collection is made out of 21 specimens. Our results could be more insightful and accurate with a larger selection of specimens, especially with those with high BV/TV (at present, only one specimen possesses BV/TV beyond 0.3%).
In addition, trabecular microarchitecture has not been quantified. Parameters such as connectivity density (CD), degree of anisotropy (DA), trabeculae number (Tb.N), trabeculae thickness (Tb.Th), trabeculae separation (Tb.Sp), and structure model index (SMI) could be used to provide mechanistic insight into trabecular bone mechanical behavior. The quasi-nonlinear FE brittle analysis was designed with an incremental step of 0.05%. We might gain an increase in results precision by assigning a scaled down incremental step.

Concerning the FE models, since the whole specimen immediately reach the ultimate point without the feasibility to capture yield point, we have to keep in mind that we compare predicted values corresponding to the ultimate point at the apparent level for the brittle model, and to the yield point for the ductile model.
Lastly, the impact of large-deformation failure mechanisms described here may not be representative of the trabecular bone's *in situ* behavior since we used excised cubic specimens for our finite element analyses [33]. Since an interruption in connectivity occurs at the sides of removed specimens of trabecular bone that can relatively alter apparent-level behavior [28], large-deformation failure mechanisms may arise preferentially in peripheral trabeculae in these specimens [33].

As far as trabecular bone is concerned, very limited understanding of how small-scale properties affect trabecular apparent strength is well known. Additionally, if individual trabeculae become more brittle with aging, disease, or drug treatment, how does that influence the strength of the overall trabecular bone? This multi-scale issue, which relates energy absorption or tissue ductility at one scale to load-carrying capacity or strength at a higher scale, is particularly relevant in osteoporosis applications since it is well known that with aging and drug treatments can influence tissue-level ductility and energy absorption [33, 45].
The results from this study help to illustrate some interests regarding high-resolution finite element modeling of trabecular bone post-yield tissue behavior, and determine how trabecular strength is altered when the tissue is changed from perfectly brittle to perfectly ductile — the two extremes of possible tissue-level ductility. These novel analyses are the first to account for the complex 3D geometric detail of real trabecular microarchitecture, and they identified unique behavior of trabecular bone that raises interesting questions for future research. Results apply to small trabecular bone specimens. It will be of interest to extend these analyses to whole bones.
This is the first study on trabecular bone to mechanistically link tissue-level ductility, a potentially important aspect of tissue material behavior, to the apparent-level strength, which is relevant clinically, and assess locations of the weak-link regions.

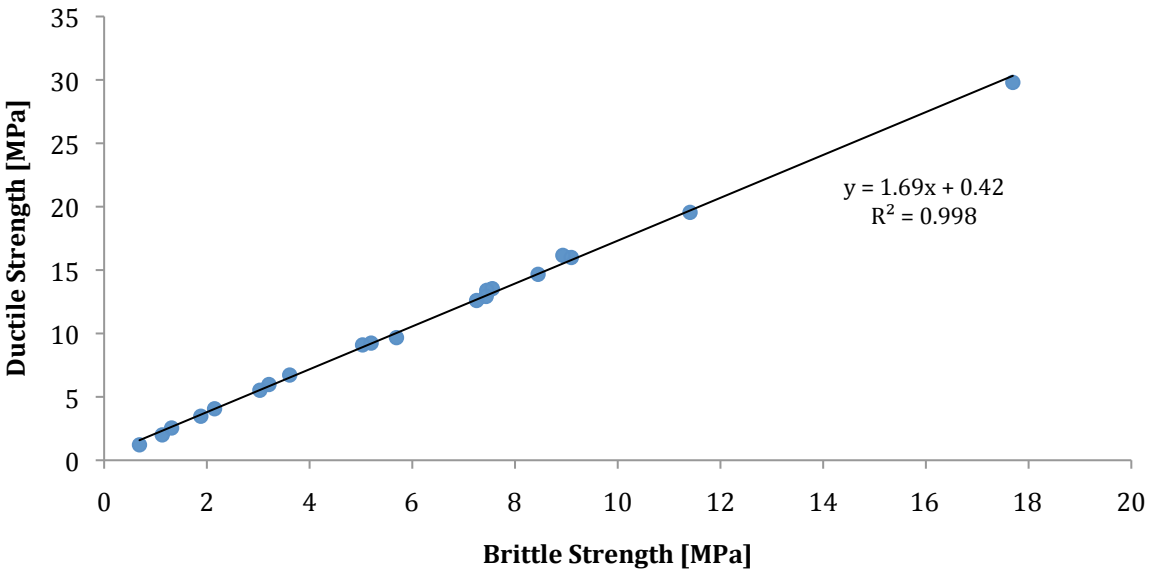

Figure 4.1. Brittle vs. Ductile predicted strength gathered at ultimate and yield points respectively. There is an obvious possibility to predict one model with the other one.

5 APPENDIX

5.1 *Drill for brittle FEA*

To run a complete analysis you will have to use in parallel the local computer in the lab (i.e. Biomech) and the Supercomputer.

(1) Open a terminal window in which you go in your specimen directory by doing:

```
[juillard@biomech ~]$ cd Damage
[juillard@biomech ~]$ cd specimenX
```

Here you should have your cube volume (i.e. `C0002714.bw.cube.5mm.227.227.227.vol.connected`),

(2) Create the first step directory (5percent if the analysis is divided into 20 steps)

```
mkdir 5pcnt
```

(3) Move the volume into 5pcnt and create the first feap file:

```
mv C0002714.bw.cube.5mm.227.227.227.vol.connected 5pcnt

~/bin/node_new_softlayer
```

A series of questions are asked and you should answer them as following:

```
[juillard@biomech specimen3]$ ~/bin/node_new_softlayer
Input data file: C0002714.bw.cube.5mm.227.227.227.vol.connected
Output file name: 5pcnt
Output FEAP file for this volume?(y/n): y
Enter the heading of FEAP file: 5pcnt
Do you want to apply load on the model?(y/n):n
Do you want to apply disp on the model?(y/n):n
Do you have many material cards?(y/n):y
Enter total number of material cards: 2
Do you have soft layers in the model?(y/n):n
Output boundary nodes for this volume?(y/n): n
Enter the size of the array
Number of pixels in the X,Y,Z directions: 227 227 227
Your bone sample is: 227 X 227 X 227
Enter the pixel dimensions (mm)
 X,Y,Z dimensions: 0.022 0.022 0.022
Enter the modulus (Mpa): 1
Enter the Poisson's ratio: 1
Enter the maximum number of iterations: 1
Enter the convergence tolerance: 1
Enter the output frequency: 1
Select the desired boundary condition:
        1.      Simple compression or tension
        2.      Confined compression or tension
        3.      Simple shear stress
        4.      Confined shear strain
```

```
        5.      Combined compressive and shear strain
Enter your selection: 1
Select the loading direction:
        1.      X
        2.      Y
        3.      Z
        4.      Done
Enter your selection: 3
Enter the Z strain in (%): -0.05
```
(because we do the step corresponding to 5% of 1% apparent strain)
```
Select the loading direction:
        1.      X
        2.      Y
        3.      Z
        4.      Done
Enter your selection: 4
```

(4) As step (3) is done you should have in your directory: `5pcnt, 5pcnt.coord`, and `5pcnt.feap`. Only the feap file interests us. Be careful that number of lines corresponds to values in the file's header. Be sure that displacement values correspond to -0.05 * specimen size. And then Zip it: `gzip 5pcnt.feap`

(5) Send it to your specimen directory in the supercomputer:

```
sftp
alromens@ranger.tacc.utexas.edu:/scratch/01203/alromens/Damage
/specimenX
     put 5pcnt.feap.gz
```

(6) Open a new terminal and login to supercomputer:

```
ssh -X alromens@ranger.tacc.utexas.edu
```

password: N58irtz6

Type `cds` to go in the right folder, and then `cd Damage`, `cd specimenX`.

Here you should see the feap file you just sent (`5pcnt.feap.gz`).

(7) Unzip it: `gunzip 5pcnt.feap.gz`

(8) You should also see the following files: `solv, mate, .petscrc, and olympus.job`

(9) Create a new directory that you call temp: `mkdir temp`

(10) Make a copy of your feap file that you will call `Img228`:

```
ln -s 5pcnt.feap Img228
```

(11) modify job name and email address in olympus.job: `vi olympus.job`

(10) run the analysis: `qsub olympus.job`

(12) Once the analysis is done, you should see many files starting with DB.
make a new directory: `mkdir DB_step1_5pcnt`
and move those files in the new one: `mv DB.* DB_step1_5pcnt`

(13) rename temp file as: `mv temp results_step1_5pcnt`

(14) go in the new file `results_step1_5pcnt` and erase files starting with I, L or F:

```
rm -rf I* L* F*
```

(15) you should see then only files starting with `0_a`... Run both commands:

```
grep Pr.Sum O_a* > prsum
gawk -f ~/bin/reacnonlin.gawk prsum > F1
```
that will add stresses in z direction of each element at the bottom surface. The file `F1` will contain the average reaction force [N] applied on the bottom surface.

(16) Run the command: `~/bin/sigeps_nl`

Here is what you should see in your `results_step_i` file:

```
O_a0of16_0     O_a11of16_0   O_a13of16_0   O_a15of16_0   O_a2of16_0
O_a4of16_0  O_a6of16_0  O_a8of16_0  prsum  sig2
O_a10of16_0    O_a12of16_0   O_a14of16_0   O_a1of16_0     O_a3of16_0
O_a5of16_0  O_a7of16_0  O_a9of16_0  sig1
```

(16) send `sig1` and `sig2` to local computer in the 5pcnt file:

```
scp                                                          sig*
juillard@biomech.me.berkeley.edu:/mnt/disk2/home2/juillard/Damage/specimenX/5pcnt
```

(17) Run either the command: `~/bin/procsigfull_cubenl.sh` (if resolution is 22 microns)

Or: `sh ~/bin/procsigfull_20nl.sh` (if resolution is 20 microns)

You should then see additional files in your directory:

```
nohup.out  princsig1  princsig2  princsigall  sig1  sig1out  sig2
sig2out  5pcnt.feap  wc_sig1out  wc_sig2out  wc_sigallout
```

(18) Run the command:

```
nohup sh ~/bin/nlsigfinalrepscript3m2.sh >& log_sfrs
```

Additional files are created.

Be sure to have the IDL script `newvol.pro` in the directory.

This script will extract failed elements in tension and compression from `sigelemfail_ten` and `sigelemfail_comp` and create a new volume with different voxel value for those elements.

(19) Start IDL, and run:

```
newvol,'          C0002714.bw.cube.5mm.227.227.227.vol.connected','
C0002714.bw.step1.5mm.227',227,227,227
```

(20) You should now have a new volume. Make a new feap file as in step (3), but this time enter the new volume as the first parameter asked, call that new feap file 10pcnt, and apply 0.1% displacement .

You can check if the script has run properly with command:

`wc -l your_file`, that will return the number of lines in that file. You should thus be sure that 5pcnt.feap and 10pcnt.feap have the same number of lines.

(21) Now that you have the new feap file, zip it and send it back to the supercomputer and so on from step (4).

5.2 *Drill for ductile FEA*

(1) Open a terminal window in which you go in your specimen directory by doing:

```
[juillard@biomech ~]$ cd Damage
[juillard@biomech ~]$ cd specimenX
```

Here you should have your cube volume (i.e. `C0002714.bw.cube.5mm.227.227.227.vol.connected`),

(2) Create the feap file corresponding to the above volume: `~/bin/node_new_softlayer`
A series of questions are asked and you should answer them as following:

```
Input data file: C0002714.bw.cube.5mm.227.227.227.vol.connected
Output file name: nonlin_100pcnt
Output FEAP file for this volume?(y/n): y
Enter the heading of FEAP file: nonlin_100pcnt
Do you want to apply load on the model?(y/n):n
Do you want to apply disp on the model?(y/n):n
Do you have many material cards?(y/n):y
Enter total number of material cards: 2
Do you have soft layers in the model?(y/n):n
Output boundary nodes for this volume?(y/n): n
Enter the size of the array
Number of pixels in the X,Y,Z directions: 227 227 227
Your bone sample is: 227 X 227 X 227
Enter the pixel dimensions (mm)
 X,Y,Z dimensions: 0.022 0.022 0.022
Enter the modulus (Mpa): 1
Enter the Poisson's ratio: 1
Enter the maximum number of iterations: 1
Enter the convergence tolerance: 1
Enter the output frequency: 1
Select the desired boundary condition:
        1.      Simple compression or tension
        2.      Confined compression or tension
        3.      Simple shear stress
        4.      Confined shear strain
        5.      Combined compressive and shear strain
Enter your selection: 1
Select the loading direction:
        1.      X
        2.      Y
        3.      Z
        4.      Done
Enter your selection: 3
Enter the Z strain in (%): -1
```

(because we do only 1 step corresponding to compressive 1% apparent strain)

```
Select the loading direction:
        1.      X
        2.      Y
        3.      Z
        4.      Done
Enter your selection: 4
```

(3) Zip the .feap file and send it to your specimen directory in the supercomputer:

```
sftp
alromens@ranger.tacc.utexas.edu:/scratch/01203/alromens/Nonlin
_cube/specimenX
```
and
```
put nonlin_100pcnt.feap.gz
```

(4) Open a new terminal and login to supercomputer:
`ssh -X alromens@ranger.tacc.utexas.edu`
password: N58irtz6

(5) Type `cds` to go in the right folder, and then `cd Nonlin_cube`, `cd specimenX`. Here you should see the feap file you just sent (`nonlin_100pcnt.feap.gz`).

(6) Unzip it: `gunzip nonlin_100pcnt.feap.gz`

(7) You should also see the following files: `solv`, `mate`, `.petscrc`, and `olympus.job`

(8) Create a new directory that you call temp: `mkdir temp`

(9) Make a copy of your .feap file that you will call `Img64`:
```
ln -s nonlin_100pcnt.feap Img64
```

(10) Modify job name, and email address in olympus.job: `vi olympus.job`

(11) Run the analysis: `qsub olympus.job`

(12) Once the analysis is done, you should see many files starting with DB.
Make a new directory: `mkdir DB64`
and move those files in the new one: `mv DB.* DB64`

(13) Rename temp file as: `mv temp results64`

(14) Go in the new file `results64` and erase files starting with I, L or F:
```
rm -rf I* L* F*
```

(15) You should see then only files starting with `O_a`... Run both commands:
```
grep Pr.Sum O_a* > prsum
gawk -f ~/bin/reacnonlin.gawk prsum > FspecX
```
that will add stresses in z direction of each element at the bottom surface. The file `FspecX` will contain the average reaction force [N] applied on the bottom surface for 20 steps going from 0% to 1% apparent strain.

(16) Transfer `FspecX` to Juillard directory:

```
scp                                                              FspecX
juillard@biomech.me.berkeley.edu:/home2/disk2/juillard
```

(17) Open matlab in the directory where `FspecX` is situated: `matlab -nodesktop`

(18) Run both commands:
```
a=load('FspecX')
yielddatta(a)
```

(19) You should see a text file with a yield value. Copy that value into `nfail.awk` in the bin of supercomputer at second line of the script. Also enter the number of elements corresponding to the specimen at the 4th line. This value can be found at the top of the .feap file.

(20) Run in the specimen's directory in supercomputer the following command:
```
awk -f ~/bin/nfail.awk SGE_out… > tissufail_specX
```

(21) In the text file `tissufail_specX`, you can see number of failed elements in tension and compression at 20 steps, gradually increased from 0% to 1% apparent strain.

5.3 *Pre-Failure Toughness*

Toughness is the ability of a material to absorb energy and plastically deform without fracturing [47]. It is also defined as the resistance to fracture of a material when stressed [46]. Pre-failure toughness was determined by calculating the area underneath stress-strain curves until fracture point.

We conclude from Figure 5.3.1 that toughness prior to fracture is dependent on to BV/TV, which is a confirmation of the literature [46]. We also know that toughness is supposed to be linked to strength. This affirmation can be visualized on Figure 5.3.2. Toughness and strength must have same gradients when compared to BV/TV in order to get such constant ratios observed on Figure 5.3.2. We recorded a mean ratio between ductile and brittle toughness approaching 3.5. Since the mean ratio between ductile and brittle bone strength is equal to 1.79, we assume that the mean ratio between toughness and strength is approximately 2.

T_B = toughness in brittle analysis
T_D = toughness in ductile analysis
S_B = brittle strength
S_D = ductile strength

On Figure 5.3.3, we calculate the ratio T_D / T_B.
We know from Figure 5.3.2 that $T_D/S_D = 0.4933$, and $T_B/S_B = 0.2531$
And from Figure 3 that $S_D/S_B = 1.79$

Then $T_D / T_B = (S_D*0.4933) / (S_B*0.2531) = 1.95* (S_D/S_B) = 1.95*1.79 = 3.49$, which is the same mean value that we obtain from Figure 5.3.3

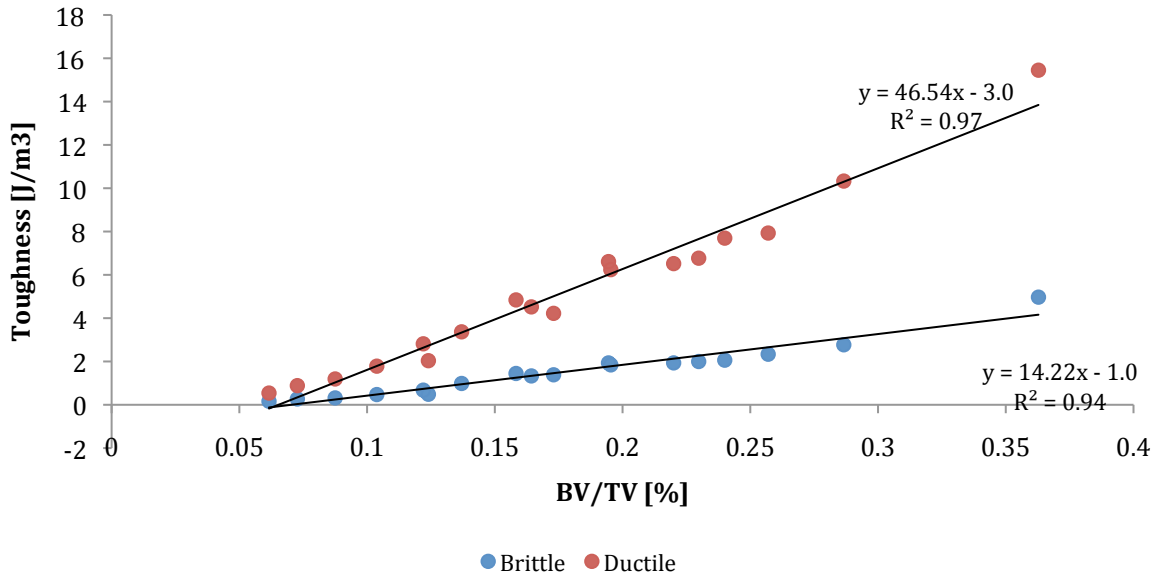

Figure 5.3.3. Toughness vs. BV/TV for both FEA, for the whole range of specimens.

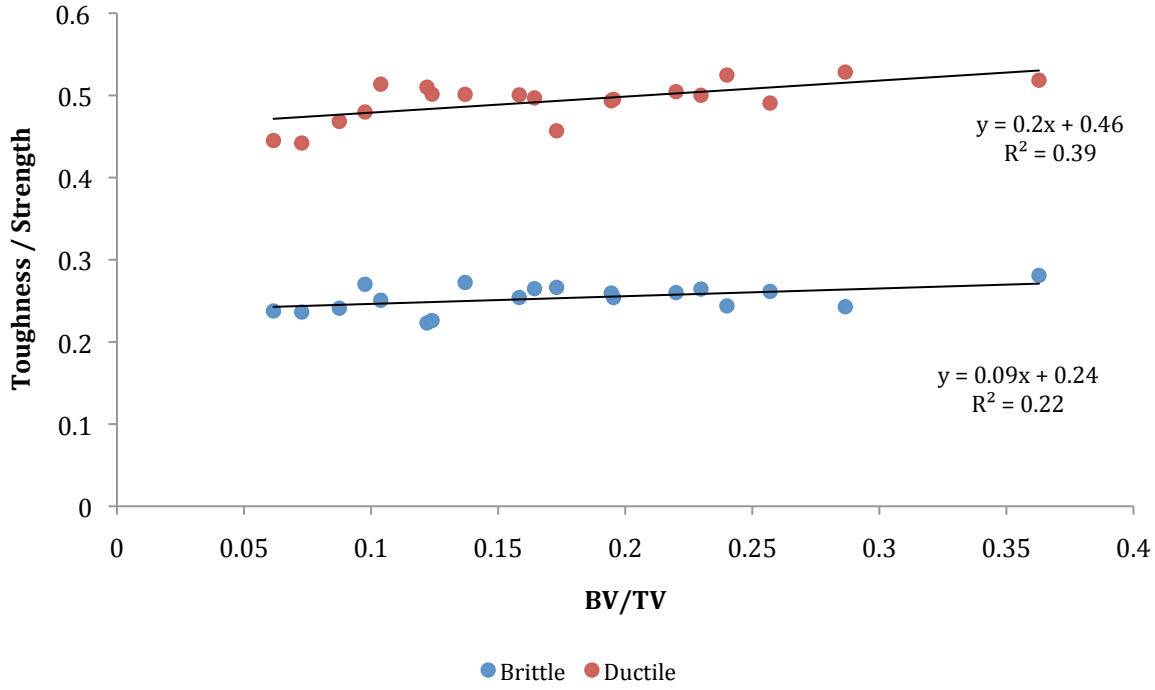

Figure 5.3.4. Ratio between toughness and yield or ultimate strength vs. BV/TV.

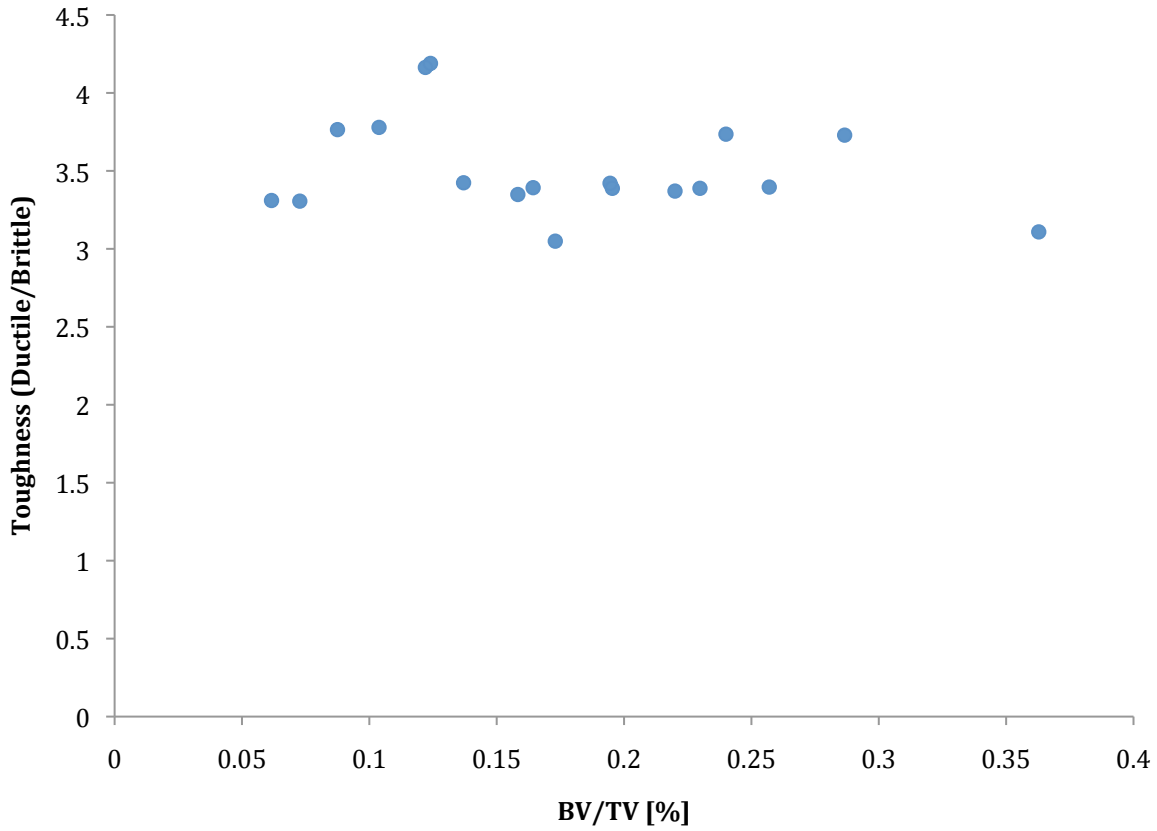

Figure 5.3.5. Ratio between ductile and brittle predicted toughness values vs. BV/TV.

6 REFERENCES

[1] Bartel, D.L, D.T. Dary and T.M. Keaveny. Orthopaedic Biomechanics: Mechanics and Design in Musculoskeletal Systems. 2007

[2] B. L. Riggs, Overview of osteoporosis. West J Med. 1991 January; 154(1): 63–77.

[3] Bevill G, Eswaran SK, Gupta A, Papadopoulos P, Keaveny TM. *Influence of bone volume fraction and architecture on computed large-deformation failure mechanisms in human trabecular bone.* Bone 2006; 39: 1218-25.

[4] National Osteoporosis Foundation. http://www.nof.org/. In. Washington, D.C.; 2008.

[5] Riggs, B.L. and L.J. Melton, 3rd, *Bone turnover matters: the raloxifene treatment paradox of dramatic decreases in vertebral fractures without commensurate increases in bone density.* J Bone Miner Res, 2002. **17**(1): p. 11-4.

[6] Heaney, R.P., *Is the paradigm shifting?* Bone, 2003. **33**(4): p. 457-65.

[7] Hernandez CJ, Keaveny TM. *A biomechanical perspective on bone quality*. Bone 2006; 39: 1173-81.

[8] Delmas PD. How does antiresorptive therapy decrease the risk of fracture in women with osteoporosis? Bone 2000;27: 1-3.

[9] Kopperdahl DL, Keaveny TM. *Yield strain behavior of trabecular bone.* Journal of Biomechanics 1998;31: 601-8.

[10] Linde F, Hvid I. *The effect of constraint on the mechanical behaviour of trabecular bone specimens*. Journal of Biomechanics 1989;22: 485-90.

[11] Cummings SR, Karpf DB, Harris F, Genant HK, Ensrud K, LaCroix AZ, Black DM.

Improvement in spine bone density and reduction in risk of vertébral fractures during treatment with antiresorptive drugs. American Journal of Medicine 2002;112: 281-289.

[12] Delmas PD, Li Z, Cooper C. *Relationship between changes in bone mineral density and fracture risk reduction with antiresorptive drugs: some issues with meta-analyses.* Journal of Bone and Mineral Research 2004;19: 330-7.

[13] Delmas PD, Seeman E. *Changes in bone mineral density explain little of the reduction in vertebral or nonvertebral fracture risk with anti-resorptive therapy*. Bone 2004;34: 599-604.

[14] Cummings SR, Bates D, Black DM. *Clinical use of bone densitometry – Scientific review.* Jama-Journal of the American Medical Association 2002;288: 1889-1897.

[15] Schuit SC, van der Klift M, Weel AE, de Laet CE, Burger H, Seeman E, Hofman A, Uitterlinden AG, van Leeuwen JP, Pols HA. *Fracture incidence and association with bone mineral density in elderly men and women: the Rotterdam Study*. Bone 2004;34: 195-202.

[16] Delmas, P.D. and E. Seeman, *Changes in bone mineral density explain little of the reduction in vertebral or nonvertebral fracture risk with anti-resorptive therapy.* Bone, 2004. **34**(4): p. 599-604.

[17] Bell, G.H., O. Dunbar, J.S. Beck, and A. Gibb, *Variations in strength of vertebrae with age and their relation to osteoporosis.* Calcified Tissue Research, 1967. **1**(1): p. 75-86.

[18] Snyder, B.D., S. Piazza, W.T. Edwards, and W.C. Hayes, *Role of trabecular morphology in the etiology of age-related vertebral fractures.* Calcified Tissue International, 1993. **53S**(1): p. S14-S22.

[19] Kanis JA, Melton LJ, Christiansen C, Johnston CC, Khaltaev N. *The diagnosis of*

osteoporosis. Journal of Bone and Mineral Research 1994;9: 1137-1141.

[20] Boutroy S, van Rietbergen B, Sornay-Rendu E, Munoz F, Bouxsein ML, Delmas PD. *Finite Element Analyses Based on In Vivo HR-pQCT Images of the Distal Radius is Associated with Wrist Fracture in Postmenopausal Women.* Journal of Bone and Mineral Research 2007.

[21] Gibson, L.J., *The mechanical behavior of cancellous bone.* Journal of Biomechanics, 1985. **18**(5): p. 317-328.

[22] Müller, R., S.C. Gerber, and W.C. Hayes, *Micro-compression: a novel technique for the nondestructive assessment of local bone failure.* Technology and Health Care, 1998. **6**(5-6): p. 433-44.

[23] Morgan, E.F., H.H. Bayraktar, O.C. Yeh, and T.M. Keaveny, *Contribution of inter-site variations in architecture to trabecular bone apparent yield strain.* Journal of Biomechanics, 2003. **37**(9): p. 1413-1420.

[24] Niebur, G.L., M.J. Feldstein, J.C. Yuen, T.J. Chen, and T.M. Keaveny, *Highresolution finite element models with tissue strength asymmetry accurately predict failure of trabecular bone.* Journal of Biomechanics, 2000. **33**: p. 1575-1583.

[25] Bevill, G., S.K. Eswaran, A. Gupta, P. Papadopoulos, and T.M. Keaveny, *Influence of Bone Volume Fraction and Architecture on Computed Large-Deformation Failure Mechanisms in Human Trabecular Bone.* 2005

[26] Biomechanics, ETHZ, http://www.biomechanics.ethz.ch/osteoporosis.php

[27] Guglielmi G, Gluer CC, Majumdar S, Blunt BA, Genant HK. *Current methods and advances in bone densitometry.* European Journal of Radiology 1995; 5: 129-39.

[28] Un K, Bevill G, Keaveny TM. *The effects of side-artifacts on the elastic modulus of trabecular bone*. Journal of Biomechanics 2006; 39: 1955-63.

[29] Morgan EF, Yeh OC, Chang WC, Keaveny TM. *Nonlinear behavior of trabecular bone at small strains*. Journal of Biomechanical Engineering 2001; 123: 1-9.

[30] Kaplan SJ, Hayes WC, Stone JL, Beaupre GS. *Tensile strength of bovine trabecular bone*. Journal of Biomechanics 1985; 18: 723-7.

[31] Bayraktar HH, Keaveny TM. *Mechanisms of uniformity of yield strains for trabecular bone*. Journal of Biomechanics 2004;37: 1671-8.

[32] Hollister SJ, Brennan JM, Kikuchi N. *A homogenization sampling procedure for calculating trabecular bone effective stiffness and tissue level stress*. Journal of Biomechanics 1994;27: 433-444.

[33] G. R. Bevill, *Micromechanical Modeling of Failure in Trabecular Bone*, 2008

[34] Bayraktar HH, Gupta A, Kwon RY, Papadopoulos P, Keaveny TM. *The modified super-ellipsoid yield criterion for human trabecular bone*. Journal of Biomechanical Engineering 2004;126: 677-84.

[35] Bourne BC, van der Meulen MC. *Finite element models predict cancellous apparent modulus when tissue modulus is scaled from specimen CT-attenuation.* Journal of Biomechanics 2004;37: 613-21.

[36] Niebur GL, Feldstein MJ, Keaveny TM. *Biaxial failure behavior of bovine tibial trabecular bone*. Journal of Biomechanical Engineering 2002; 124: 699-705.

[37] Eswaran SK, Gupta A, Keaveny TM. *Locations of bone tissue at high risk of initial failure during compressive loading of the human vertebral body*. Bone 2007;41: 733-9.

[38] Pistoia W, van Rietbergen B, Lochmuller EM, Lill CA, Eckstein F, Ruegsegger P. *Estimation of distal radius failure load with micro-finite element analysis models*

based on three-dimensional peripheral quantitative computed tomography images. Bone 2002;30: 842-8.

[39] MacNeil JA, Boyd SK. *Bone strength at the distal radius can be estimated from high resolution peripheral quantitative computed tomography and the finite element method*. Bone 2008.

[40] Morgan EF, Keaveny TM. *Dependence of yield strain of human trabecular bone on anatomic site.* Journal of Biomechanics 2001; 34: 569-577.

[41] Bayraktar HH, Morgan EF, Niebur GL, Morris GE, Wong EK, Keaveny TM. *Comparison of the elastic and yield properties of human femoral trabecular and cortical bone tissue.* Journal of Biomechanics 2004;37: 27-35.

[42] Nawathe, S, Juillard F, Keaveny TM, *Effects of Tissue-Level Ductility on Trabecular Bone Strength*. 2011.

[43] Adams MF, Bayraktar HH, Keaveny TM, Papadopoulos P. *Ultrascalable implicit finite element analyses in solid mechanics with over a half a billion degrees of freedom.* In: ACM/IEEE Proceedings of SC2004: High Performance Networking and Computing; 2004.

[44] Harrigan TP, Jasty M, Mann RW, Harris WH. *Limitations of the continuum assumption in cancellous bone*. Journal of Biomechanics 1988; 21: 269-75.

[45] Turner Ch, *Biomechanics of bone: determinants of skeletal fragility and bone quality.* Osteoporos Int. 2002; 13(2): 97-104.

[46] Zioupos, P, *Recent developments in the study of failure of solid biomaterials and bone: 'fracture' and 'pre-fracture' toughness*. Material Science and Engineering 1998 ; volume 6 : 33-40.

[47] Wikipedia : http://en.wikipedia.org/wiki/